# HD 213885b: A transiting 1-day-period super-Earth with an Earth-like composition around a bright ($V = 7.9$) star unveiled by TESS

Néstor Espinoza[1,2]★†‡, Rafael Brahm[3,4,6], Thomas Henning[2], Andrés Jordán[5,6], Caroline Dorn[7], Felipe Rojas[4,5], Paula Sarkis[2], Diana Kossakowski[2], Martin Schlecker[2], Matías R. Díaz[8], James S. Jenkins[8], Claudia Aguilera-Gomez[9], Jon M. Jenkins[10], Joseph D. Twicken[11], Karen A. Collins[12], Jack Lissauer[10], David J. Armstrong[13,14], Vardan Adibekyan[15], David Barrado[16], Susana C. C. Barros[15], Matthew Battley[13,14], Daniel Bayliss[13,14], François Bouchy[17], Edward M. Bryant[13,14], Benjamin F. Cooke[13,14], Olivier D. S. Demangeon[15], Xavier Dumusque[17], Pedro Figueira[18,14], Helen Giles[17], Jorge Lillo-Box[18], Christophe Lovis[17], Louise D. Nielsen[17], Francesco Pepe[17], Don Pollacco[13], Nuno C. Santos[15,19], Sergio G. Sousa[15], Stéphane Udry[17], Peter J. Wheatley[13,14], Oliver Turner[17], Maxime Marmier[17], Damien Ségransan[17], George Ricker[20], David Latham[12], Sara Seager[20], Joshua N. Winn[21], John F. Kielkopf[22], Rhodes Hart[23], Geof Wingham[24], Eric L. N. Jensen[25], Krzysztof G. Hełminiak[26], A. Tokovinin[27], C. Briceño[27], Carl Ziegler[28], Nicholas M. Law[29], Andrew W. Mann[29], Tansu Daylan[19]§, John P. Doty[30], Natalia Guerrero[19], Patricia Boyd[31], Ian Crossfield[20], Robert L. Morris[11,10], Christopher E. Henze[10], Aaron Dean Chacon[32,10]

*The authors' affiliations are shown in Appendix A.*

**ABSTRACT**

We report the discovery of the 1.008-day, ultra-short period (USP) super-Earth HD 213885b (TOI-141b) orbiting the bright ($V = 7.9$) star HD 213885 (TOI-141, TIC 403224672), detected using photometry from the recently launched *TESS* mission. Using FEROS, HARPS and CORALIE radial velocities, we measure a precise mass of $8.8 \pm 0.6 M_\oplus$ for this $1.74 \pm 0.05 R_\oplus$ exoplanet, which provides enough information to constrain its bulk composition — similar to Earth's but enriched in iron. The radius, mass and stellar irradiation of HD 213885b are, given our data, very similar to 55 Cancri e, making this exoplanet a good target to perform comparative exoplanetology of short period, highly irradiated super-Earths. Our precise radial velocities reveal an additional 4.78-day signal which we interpret as arising from a second, non-transiting planet in the system, HD 213885c, whose minimum mass of $19.9 \pm 1.4 M_\oplus$ makest it consistent with being a Neptune-mass exoplanet. The HD 213885 system is very interesting from the perspective of future atmospheric characterization, being the second brightest star to host an ultra-short period transiting super-Earth (with the brightest star being, in fact, 55 Cancri). Prospects for characterization with present and future observatories are discussed.

**Key words:** planets and satellites: detection — planets and satellites: fundamental parameters — planets and satellites: individual: TOI-141, TIC 403224672, HD213885 — planets and satellites: terrestrial planets — techniques: photometric — techniques: radial velocities

arXiv:1903.07694v2 [astro-ph.EP] 4 Nov 2019

## 1 INTRODUCTION

The successfully launched and currently operating Transiting Exoplanet Survey Satellite (TESS, Ricker et al. 2015) is set to become one of the most important missions in the search for small, characterizable rocky exoplanets. Currently exploring almost the whole sky on the hunt for transiting exoplanets orbiting bright ($V < 13$) stellar hosts, TESS' primary mission is to generate a sample of small ($< 4R_\oplus$) exoplanets for which precise masses and even atmospheric characterization will be possible, revolutionizing our view of these small, distant worlds.

Among the distinct populations of small exoplanets, one of the most interesting are the so-called Ultra-Short-Period (USP) exoplanets. These are planets that orbit at extremely short periods ($P \leq 1$ day), smaller than about $2R_\oplus$, and which appear to have compositions similar to that of the Earth (Winn et al. 2018). Although almost a hundred of these systems have been found by the *Kepler* mission, with which it was found that these exoplanets are extremely rare (about as rare as hot-jupiters, Sanchis-Ojeda et al. 2014), only a handful of them have precise radii and masses, as the stars in the *Kepler* field are typically much too faint for spectroscopic follow-up. Transit surveys like TESS, however, are the perfect haystacks to find these rare needles as they are designed to find short-period transiting exoplanets around bright stellar hosts, allowing us to explore the yet poorly understood dimension of mass and, thus, bulk composition of these interesting extrasolar worlds. In addition, missions like TESS are extremely important for exoplanets such as USPs as they will generate a sample of them which will be prime targets for future atmospheric follow-up with missions like the upcoming James Webb Space Telescope (JWST), which will in turn allow us to explore the exciting dimension of atmospheric composition of these small, short-period exoplanets (see, e.g., the case of 55 Cancri e; Demory et al. 2016; Angelo & Hu 2017; Miguel 2019).

The possibility to perform spectroscopic follow-up for these USPs is in turn also interesting because of another fact: the inclination between the orbits of multi-planetary systems appears to be larger for short-period exoplanets in tight orbits ($\Delta i = 6.7 \pm 0.6$ degrees for planets with $a/R_* \leq 5$ versus $2.0 \pm 0.1$ for planets with $5 < a/R_* < 12$, Dai et al. 2018), which might be a signature of orbital migration due to excitation effects such as high-eccentricity migration (Petrovich et al. 2018). If this effect is indeed the one dominating in systems having USPs, then detecting transits of more than one planet in multi-planetary systems might be intrinsically harder to do than for systems not having them, as the increased mutual inclination between the exoplanets in the system might prevent us from observing the transits of the other members of it. However, if their inclinations are within the same order of magnitude, these extra members might be found via high-precision spectroscopic follow-up, and this might in turn provide valuable constraints on the mutual inclinations between the exoplanets of these systems that might aid in the understanding of the formation of these rare, small exoplanets.

In this work, we present the discovery and characterization of **a new** USP discovered by the TESS mission, HD 213885b (TOI-141b), characterized thanks to precise radial-velocity measurements from FEROS, HARPS and

‡ IAU-Gruber Fellow
§ Kavli Fellow

CORALIE. In addition to the tight constraint on the mass of this new exoplanet, our radial-velocity measurements reveal the presence of an additional non-transiting exoplanet in the system, HD 213885c (TOI-141c).

We organize this work as follows. In Section 2 we present the data used to make the discovery of this multi-planet system. In Section 3 we present the analysis of this data, in which we derive the properties of both the star and the planets in the system. In Section 4 we present a discussion on the system and the implication of this discovery to both the overall population of small exoplanets and the known USPs and in Section 5 we present the conclusions of our work.

## 2 DATA

### 2.1 TESS photometry

TESS photometry for TOI-141 was obtained in short-cadence (2-minute) integrations from July 2018 to August 2018 (during a total time-span of 27.9 days) in TESS Sector 1 using Camera 2. The TESS Science Processing Operations Center (SPOC) photometry was retrieved from the alerts webpage[1], which provide either simple aperture photometry (`SAP_FLUX`) or the systematics-corrected photometry (`PDCSAP_FLUX`), a procedure performed by an adaptation of the Kepler Presearch Data Conditioning algorithm (PDC, Stumpe et al. 2012; Smith et al. 2012; Stumpe et al. 2014) to TESS. We use this latter photometry along with its provided errorbars (`PDCSAP_FLUX_ERR`) in the rest of this work; we refer to this photometry as the PDC photometry in what follows. Both, the SAP and PDC median-normalized photometry provided by the TESS alerts are presented in Figure 1. For the analysis that follows, we remove two portions of the data: the portion (in BJD - 2457000) between 1347.5 and 1349.3, which was obtained during a period of increased spacecraft pointing jitter (see Huang et al. 2018), and the region after 1352, which shows an evident relatively short but significant decrease in flux which we found might give rise to biases in our analysis.

The TESS alerts diagnostics, generated using the tools outlined in Twicken et al. (2018), Jenkins et al. (2016) and Li et al. (2019) which have been adapted to work with TESS data, present this system as having a 1-day transit signal present in the data, which we refer to as TOI-141.01. The transit signature of this planet passes all the Data Validation (DV) tests (e.g., comparison of even and odd transits to screen against eclipsing binaries, ghost diagnostic tests to help rule out scattered light or background eclipsing binaries, among others) but the difference image centroiding test, likely due to the star being slightly saturated. From a difference image analysis done within the DV, however, the transit source is coincident with the core of the stellar point spread function (PSF), so it is clear the transit events happen on the target and not in, e.g., nearby bright stars. In order to confirm this signal and search for additional ones in the photometry, we ran the Box Least-Squares algorithm (BLS, Kovács et al. 2002) on the data using a `python` implementation of this algorithm by Daniel Foreman-Mackey,

`bls.py`[2]. Significances of the possible peaks were computed by running the algorithm on a mock dataset, which contained the same median flux as the TESS photometry, and to which we added white-gaussian noise whose standard-deviation was defined as the provided errorbars at each time-stamp. This procedure was ran 100 times, giving 100 BLS powers at each period, with which the mean BLS power and the corresponding standard deviation at each period was calculated. A peak in the BLS spectrum of the original data was then considered significant and was later inspected if it deviated by more than 5-sigma from this white-gaussian noise spectrum. We ran the BLS on the search of transits with periods between 0.1 and 14 days (the latter chosen as around half the total time-span of the TESS observations; 5,000 periods were considered between those limits), searching for transits with durations between $q = 0.01$ and $q = 0.09$ in phase-space.

Using the BLS on the PDC photometry, the largest peak in the BLS periodogram was located at around the same period as the one reported on the TESS alerts, i.e., at 1.007 days, with a depth of around 200 ppm. The peak is highly significant — greater than 100 standard deviations above the mean BLS power at this period. It is interesting to note that the transits of this planetary candidate are individually visible in the lightcurve of TOI-141 presented in Figure 1, indicated in that figure by red lines. We removed the in-transit points corresponding to TOI-141.01 and repeated the same procedure on the masked data. A couple of peaks emerge in the BLS periodogram just above our 5-sigma threshold, but when phasing the data at those periods, no evident transit signature emerges. In addition, those peaks are only at specific periods, and thus very narrow (one or two points) in the BLS periodogram. We thus conclude that no more significant transit-like signals are present in the BLS periodogram of our data. Possible additional signals in the photometry were also inspected using the Transiting Planet Search (TPS) within the SPOC Data Validation (DV) component, which as mentioned above has been recently adapted to work with TESS data (Twicken et al. 2018; Jenkins et al. 2016; Li et al. 2019). No additional transiting planets were found with those tools either.

It is important to note that the aperture used to obtain the TESS photometry encompasses about 3 TESS pixels in radius around the target, which amounts to an on-sky aperture of about 1 arcminute which in turn could lead to the light of other stars to contaminate the aperture. This could in turn give rise to possible dilutions of the observed transits, which could lead to misdetermination of the transit parameters, and to possible false-positives, which could led us to believe this is an exoplanetary system when in reality the observed TESS transit events could be due to a blend with a nearby eclipsing binary. In particular, the TESS aperture includes light not only from TOI-141 (which has a TESS magnitude of $7.358 \pm 0.018$), but also from five nearby stars: two faint stars, which we denote C1 and C2 in what follows, at about 30 arcseconds from the target detected by both 2MASS (2MASS IDs: 22360031-5952070 and 22355219-5952034, for C1 and C2, respectively) and Gaia (Gaia Source IDs 6407428925971511808 and 6407428960331344512, for C1

---

[1] https://tess.mit.edu/alerts/

[2] https://github.com/dfm/bls.py

and C2, respectively; Gaia Collaboration et al. 2018)), and three additional stars fainter than C1 and C2 by Gaia (Gaia Source IDs: 6407428891610548736, 6407428925970566272 and 6407434801486912768), the brightest of which has a Gaia magnitude of $G = 19.86$ — implying a $\Delta G = 12.1$ with TOI-141.

Assuming the magnitude difference in the TESS passband to be similar to the difference in the Gaia passband, the three faint stars detected by Gaia and not 2MASS are negligible sources of light in practice to the TESS aperture (if any of these were a totally eclipsing binary, for example, they would lead to transit depths of about 15 ppm; in terms of lightcurve dilution, they amount to less than 0.0015% of the light in the aperture). For C1 and C2, using the relations in Stassun et al. (2018), their TESS magnitudes are $T_{C1} = 16.862 \pm 0.025$ and $T_{C2} = 16.417 \pm 0.023$ respectively (calculated using the 2MASS $J$ and Gaia $G$ magnitudes of these stars, which are the magnitudes that have the smaller errorbars, and propagating the errors on the relations of Stassun et al. (2018) in quadrature to the photometric errors). This implies a magnitude difference with TOI-141 in the TESS passband of $9.504 \pm 0.031$ and $9.059 \pm 0.029$ for C1 and C2 respectively, thus amounting for 0.041% of the light in the TESS aperture. If any of those stars were to produce the observed transits in the TESS photometry of TOI-141.01, they would have to be variable objects producing periodic 1-day dimmings of at least 80% of their light. We explore this possibility with follow-up lightcurves in the next sub-section.

## 2.2 Photometric follow-up

Photometric follow-up was performed as part of the TESS Follow-up Program (TFOP) SG1 Group. We used the `TESS Transit Finder`, which is a customized version of the `Tapir` software package (Jensen 2013), to schedule photometric time-series follow-up observations. Observations of TOI-141.01 were obtained on September 11, 2018, using the CDK700 27-inch telescope at Mount Kent Observatory (MKO). The observations were made in $r'$ using 128 second "deep" exposures, effectively saturating TOI-141 but gathering enough photons to provide precise photometry for the fainter companion stars in order to rule-out false-positive scenarios. The observations covered around 3 hours, and effectively covered the predicted ingress and egress events. We used AstroImageJ (Collins et al. 2017) to calibrate the data and extract the differential aperture photometry of the target and nearby stars. All stars within $2'$ turned out to have a constant brightness to within 10%. Dimmings at the 80% or larger for C1 and C2 can be confidently ruled out by these observations; however, C1 showed a 70% *rise* in the photometry around the expected mid-transit time of TOI-141.01, which was due to an instrumental effect: due to the rotation of the field, some of the diffraction spikes of TOI-141 fell on the aperture used to extract the photometry of C1 at these times generating this increase in the relative flux of this object. It is important to stress here that although mid-transit was lost due to this effect, the lightcurve before this event showed no large variations as the ones expected from an eclipsing binary causing the TESS transits (the precise transit ephemerides for this system ensure we should have caught at least an ingress event if this was indeed an eclipsing binary).

The observations presented above thus rule out any possible near eclipsing binary as being the responsible for the transit events observed in the TESS lightcurve.

## 2.3 Speckle imaging

Speckle imaging for TOI-141 was obtained on September 24, 2018, using the High-Resolution Camera (HRCam) at the 4.1m Southern Astrophysical Research (SOAR) telescope located in Cerro Pachón, Chile, in the $I$-band; the co-added images are presented in Figure 2. The instrument and the corresponding analysis and reductions of data obtained with it is detailed in Tokovinin (2018). These observations, and the subsequent analysis of the auto-correlation function (ACF) of the image, which provides better dynamic range than working on the images directly (see Tokovinin 2018, for details), reveal 2 companions to TOI-141: one at a separation of 1.19" from TOI-141 at an angle of 305 degrees, and another at a separation of 0.4" from the target at 239 degrees, with magnitude differences of $\Delta I = 5.4$ and $\Delta I = 4.9$ respectively. As will be shown in Section 3, given the observed radial-velocity variations in phase with the transit ephemerides observed by TESS — and given these companion stars are too faint to produce any measurable signal in our radial-velocity measurements — it is very unlikely the companion stars revealed by these speckle imaging observations are the ones producing the transit events. These stars, however, could be important to constrain the possible transit dilutions they imply for our target. However, given these objects are not detected in Gaia DR2 (Gaia Collaboration et al. 2018), and that only one-band observations are available, we cannot calculate either if they are physically bound nor their predicted TESS magnitudes in order to calculate the dilution these stars would imply in the TESS bandpass. If we assume the delta-magnitudes in $I$ band are similar to the TESS magnitudes, then these stars would account for about 1.8% of the total flux in the TESS aperture. For a 200 ppm transit depth as the one detected by the TESS photometry for TOI-141.01, this would imply a dilution of about the same percent of this transit depth (i.e., a depth about 4 ppm smaller) — this is well below the error on the transit depth, which as it will be shown in Section 3, is on the order of 12 ppm.

It is important to notice that, because TOI-141 is a relatively close system (48 pc — see Section 3), monitoring the system via high angular resolution in the future (e.g., a few years) might reveal if these companions detected with our observations are physically associated or not to TOI-141. We encourage future observations in order to determine if this is the case.

## 2.4 FEROS radial velocities

High precision radial velocities were obtained for TOI-141 with the Fiber-fed Extended Range Optical Spectrograph (FEROS, Kaufer & Pasquini 1998) mounted at the 2.2m MPG telescope at La Silla Observatory between September and October 2018 by the Chile-MPIA group. A total of 175 RV measurements were obtained with a simultaneous ThAr calibration using 200s exposures. The RVs were
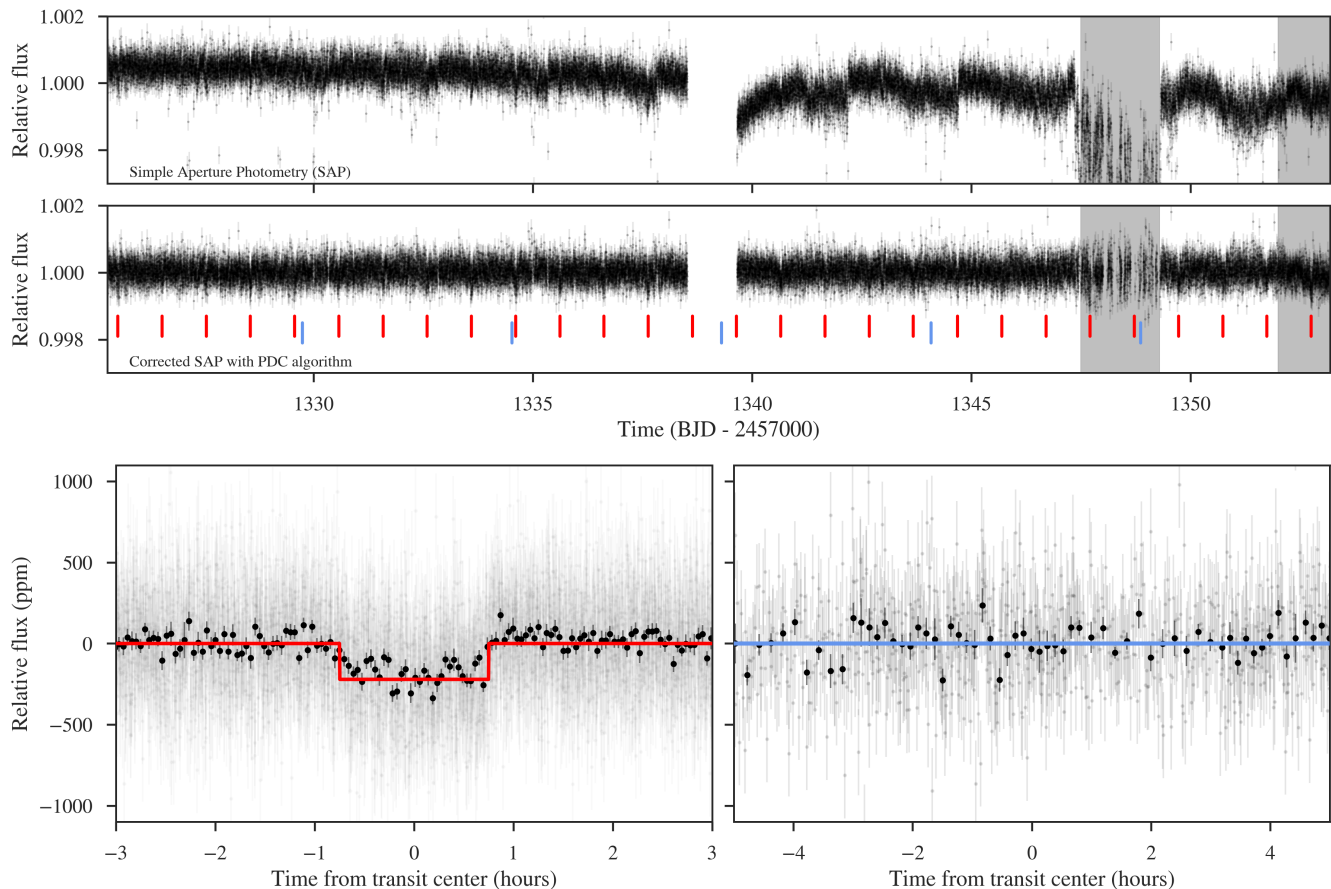
**Figure 1.** Top panels. TESS photometry for TOI-141. The upper panel shows the Simple Aperture Photometry (SAP) provided by the TESS alerts (`SAP_FLUX`) along with the corresponding errors (`SAP_FLUX_ERR`) after normalizing for the median flux. The same photometry but systematics-corrected via the PDC algorithm, also provided by the TESS alerts (`PDC_SAP_FLUX`) is shown in the bottom panel along with the corresponding errors (`PDC_SAP_FLUX_ERR`). Red lines indicate transits of the 1-day planetary candidate TOI-141.01 for which (200 ppm) transits can be easily observed by eye in the photometry. Blue lines indicate the expected position of transits of a second, 4.75-day sinusoidal signal found on the radial-velocity measurements (see Section 3.3) — no transits are evident at those times. Grey regions indicate portions of the time-series left out of our analysis (see text). Bottom panels. Phased photometry at interesting periods. The left-most phased photometry shows the photometry phased at the period of TOI-141.01 (grey points); black points show binned datapoints for visualization. Red line indicates the box model implied by our BLS search. The right panel shows the same for the 4.75-day sinusoidal signal found in our radial-velocity measurements (see Section 3.3), where the reported time of transit-center is the expected time given our radial velocities. No transit is evident.

extracted from the spectra using the customized CERES pipeline (Brahm et al. 2017a), which performs all the process of extraction from basic bias, dark and flat-field corrections (including scattered light) to order tracing, wavelength calibration and cross-correlation matching of the spectrum with templates to obtain the RVs from the spectra. Although based on standard stars the precision that the CERES pipeline obtains with FEROS is 7 m/s, we found that with some modifications to the standard acquisition of FEROS frames one can achieve 3 m/s precision for $V = 8$ stars: simply by turning the ThAr lamp around 20 minutes before it is used, and taking a long series of ThAr calibration images to select the best one as reference greatly improves the precision one can achieve with FEROS using CERES. We followed these procedures for the obtention of the RVs of TOI-141 and imposed this 3 m/s noise floor to the star based on the monitoring of standard stars.

The FEROS observations showed radial velocities in

phase with the transit ephemerides of TOI-141.01, showing an amplitude of about 5 m/s. In addition, they also showed an evident extra sinusoidal variation at a period of about 4.78-days. These signals will be analyzed in detail in Section 3. The data is presented in Table 1.

### 2.5 HARPS radial velocities

High precision radial velocities were also obtained with the High Accuracy Radial velocity Planet Searcher (HARPS) mounted at the ESO La Silla 3.6m telescope (Mayor et al. 2003). These data were obtained by three groups: the Chile-MPIA group (14 measurements in September 2018), the NCORES group (14 measurements in October 2018) and the U. de Chile group (19 measurements between October and November 2018), all of which were obtained using simultaneous ThAr calibration lamps. In total, 47 measurements were

**Table 1.** Radial-velocity measurements obtained for TOI-141.

| Time (BJD) | Radial-velocity (m/s) | Error (m/s) | Exposure time (s) | Instrument |
|---|---|---|---|---|
| 2458409.7085776 | 36164.16 | 0.56 | 900 | HARPS |
| 2458412.4991098 | 36146.57 | 0.39 | 900 | HARPS |
| 2458412.5935471 | 36149.97 | 0.46 | 900 | HARPS |
| 2458412.6969091 | 36153.13 | 0.55 | 900 | HARPS |
| ⋮ | ⋮ | ⋮ | ⋮ | |

*Note.* This table will be available in machine-readable form in the online journal. A portion is shown here for guidance regarding its form and content.
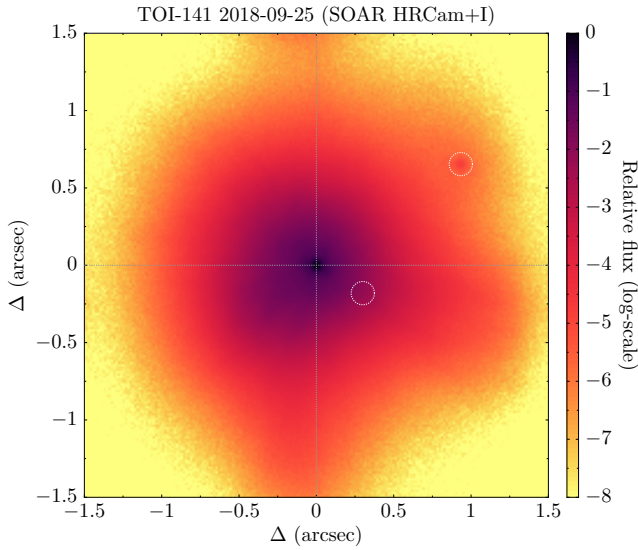


**Figure 2.** "Lucky" image obtained with the HRCam at the 4.1m SOAR telescope in the I band for TOI-141. The distant companion at 1.19" (indicated by a white circle in the figure) is evident from the image, whereas the closer 0.4" companion (also indicated) is not; this was detected via speckle ACF (see text).

obtained for TOI-141 between September 2018 and November 2018. The conditions during the September 2018 run were sub-optimal, which in turn led us to use longer exposure times on those nights of 900 seconds. Conditions were photometric for the rest of the observing runs, and so 300s exposures were used in those nights to gather spectroscopic measurements for TOI-141. The radial velocities were obtained with both the CERES pipeline (Brahm et al. 2017a) and the HARPS DRS pipeline. Although both gave consistent results, the CERES pipeline results have much larger long-term errors as monitored by standard stars than the quoted attainable precision by the DRS pipeline. Because of this, we decided to use the DRS instead of the CERES results in this work. The RV precision of those datapoints varied with the exposure times — 0.5 m/s for 900 second exposures and 2 m/s for 300 second exposures. The data is presented in Table 1.

### 2.6 CORALIE radial velocities

Additional data were obtained with the CORALIE instrument, mounted on the 1.2m Euler Telescope at the La Silla

Observatory (Queloz et al. 2001) both prior to the TESS observations and after the TESS observations. A first set of data, here denoted CORALIE07, were taken between August 2008 and October 2013 (7 radial-velocity measurements) and a second set of data, here denoted CORALIE14, were taken between August 2016 and September 2018 (8 radial-velocity measurements). From this latter set, 6 datapoints were taken after the TESS alerts were released. These datapoints have precisions between 3-4 m/s, and the radial velocities were analyzed with the official CORALIE pipeline. Two extra datapoints to the just mentioned ones were obtained in July 1990 and August 1994 by CORAVEL (Baranne et al. 1979), and another set of 12 radial-velocity datapoints were taken between September 2001 and September 2006 with CORALIE; however, we do not use those measurements in this work as they show errors in excess of the precision needed to constrain the masses of the exoplanets presented in this work. In total, thus, in this work we use 15 radial-velocity measurements from CORALIE.

It is important to note here that the CORALIE instrument was upgraded in November 2014 (see, e.g. Maxted et al. 2016). This means that the zero-point offset between the CORALIE07 and CORALIE14 radial velocities is different. Because of this reason, here we treat each as an independant dataset, meaning that in the analysis to be described in Section 3.3, we consider different systemic velocities and jitters for each of those datasets. The data is presented in Table 1.

## 3 ANALYSIS

### 3.1 Stellar properties

We followed the iterative procedure described in Brahm et al. (2018b) and Brahm et al. (2018a) to determine the physical parameters of TOI-141. First we used the co-added HARPS spectra to compute the atmospheric parameters of TOI-141 by using the ZASPE code (Brahm et al. 2017b), which compares the observed spectrum with synthetic ones in the spectral regions that are most sensitive to changes in the atmospheric parameters. Then we combined the GAIA DR2 parallax and the available photometry to compute the stellar radius and extinction using an MCMC code[3]. Finally, we determined the stellar mass and age by searching for the Yonsei-Yale evolutionary model (Yi et al. 2001) that

---

[3] https://github.com/rabrahm/rstar

matched the observed stellar radius and spectroscopic effective temperature through another MCMC code[4]. With the derived stellar mass and radius we computed a new value for the log(g) which is held fixed in a new ZASPE iteration, followed by the same steps that were just described. The final stellar parameters obtained for TOI-141 are presented in Table 2.

## 3.2 Stellar abundances

Stellar abundances are important to constrain possible interior composition models of exoplanets orbiting host stars, as they can give prior information to be used by structure modeling in order to constrain the composition of an exoplanet (see Section 4.2). Because of this, we extracted abundances from the HARPS (co-added) spectra of important refractory and volatile elements that could aid as priors in such an analysis. We use a standard LTE analysis with the 2017 version of MOOG (Sneden 1973) and Kurucz ATLAS9 model atmospheres (Castelli & Kurucz 2003), measuring the equivalent widths of Si, Ni, Mg, and C lines. The C abundance is based on two unblended lines at 5052.2 and 5380.3Å with atomic parameters from Delgado Mena et al. (2010). For Si, Ni, and Mg, the line list of Neves et al. (2009) is used instead. We found abundances $A(X) = \log_{10} N(X)/N(H) + 12$, where $N(X)/N(H)$ is the atomic ratio between element X and hydrogen (H), where $N(H)$ is normalized to $10^{12}$ hydrogen atoms (i.e., $N(H) = 12$) for Si, Ni, Mg and C — those are presented in Table 2. The errors reported consider the line-by-line scatter added in quadrature with errors produced by uncertainties on stellar parameters $T_{\rm eff}$, [Fe/H], and $\log g_*$.

## 3.3 Joint analysis

The joint analysis of the photometry and radial velocities is performed here using a new code introduced in Espinoza et al. (2018), juliet, which is available via GitHub[5]. For our analysis in this work, juliet uses batman (Kreidberg 2015) to model the transit lightcurves and radvel (Fulton et al. 2018) to model the radial velocities. juliet allows for a variety of parametrizations, and in particular allows us to incorporate Gaussian Processes (GPs) via the george (Ambikasaran et al. 2014) and celerite (Foreman-Mackey et al. 2017) packages, which are implemented within juliet for modelling underlying systematic and/or astrophysical signals present either in the radial velocities, the photometry or both, and to easily incorporate those into our modelling scheme. One of the key features of juliet is its ability to perform model comparison, as nested sampling algorithms are used to compute posterior samples and, in particular, model evidences, $Z_i$, for a model $M_i$ given the data, $\mathcal{D}$, i.e., $Z_i = p(\mathcal{D}|M_i)$. In this work within juliet we make use of MultiNest (Feroz et al. 2009) via the PyMultiNest wrapper (Buchner et al. 2014) to explore the parameter space and perform model evidence calculations. This evidence estimation in turn allows to compute the probability of the model given the data, $p(M_i|\mathcal{D}) = p(M_i)p(\mathcal{D}|M_i)$ given a prior probability for model $M_i$, $p(M_i)$. Here, unless otherwise stated, we

[4] https://github.com/rabrahm/isoAR
[5] https://github.com/nespinoza/juliet

**Table 2.** Stellar parameters of TOI-141.

| Parameter | Value | Source |
|---|---|---|
| Identifying Information | | |
| TIC ID | 403224672 | TIC |
| GAIA ID | 6407428994690988928 | Gaia DR2 |
| 2MASS ID | 22355630-5951522 | 2MASS |
| R.A. (J2015.5, h:m:s) | $22^h35^m56.09s$ | Gaia DR2 |
| DEC (J2015.5, d:m:s) | -59$^o$51'53.38'' | Gaia DR2 |
| Spectroscopic properties | | |
| $T_{\rm eff}$ (K) | $5978 \pm 50$ | ZASPE |
| Spectral Type | G | ZASPE |
| [Fe/H] (dex) | $-0.04 \pm 0.03$ | ZASPE |
| $\log g_*$ (cgs) | $4.3827^{+0.0095}_{-0.0097}$ | ZASPE |
| $v\sin(i_*)$ (km/s) | $3.0 \pm 0.2$ | ZASPE |
| $A(Si)$ (dex) | $7.48 \pm 0.09$ | MOOG |
| $A(Ni)$ (dex) | $6.19 \pm 0.11$ | MOOG |
| $A(Mg)$ (dex) | $7.51 \pm 0.06$ | MOOG |
| $A(C)$ (dex) | $8.31 \pm 0.13$ | MOOG |
| Photometric properties | | |
| $T$ (mag) | $7.358 \pm 0.018$ | TESS |
| $B$ (mag) | $8.4720 \pm 0.0020$ | APASS |
| $V$ (mag) | $7.9960 \pm 0.0020$ | APASS |
| $r'$ (mag) | $7.8500 \pm 0.0010$ | APASS |
| $i'$ (mag) | $7.7130 \pm 0.0020$ | APASS |
| $z'$ (mag) | $7.4690 \pm 0.0020$ | APASS |
| $J$ (mag) | $6.806 \pm 0.015$ | 2MASS |
| $H$ (mag) | $6.501 \pm 0.031$ | 2MASS |
| $Ks$ (mag) | $6.419 \pm 0.019$ | 2MASS |
| Derived properties | | |
| $M_*$ ($M_\odot$) | $1.068^{+0.020}_{-0.018}$ | YY* |
| $R_*$ ($R_\odot$) | $1.1011^{+0.0080}_{-0.0075}$ | Gaia DR2* |
| $L_*$ ($L_\odot$) | $1.376^{+0.045}_{-0.049}$ | YY* |
| $M_V$ | $4.462^{+0.044}_{-0.042}$ | YY* |
| Age (Gyr) | $3.80^{+0.66}_{-0.79}$ | YY* |
| Distance (pc) | $47.97 \pm 0.14$ | Gaia DR2+YY* |
| $\rho_*$ (kg m$^{-3}$) | $1127 \pm 33$ | YY* |

*Note.* Logarithms given in base 10.
*: Using stellar parameters obtained from ZASPE.

assume all models are a-priori equiprobable and thus compare model evidences directly between models as in this case the posterior odds are simply $p(M_i|\mathcal{D})/p(M_j|\mathcal{D}) = Z_i/Z_j$. For ease of comparison, we here compare models using the difference of the (natural) log-evidences, $\Delta \ln Z_{i,j} = \ln Z_i/Z_j$. We have taken care to repeat the model evidence calculations several times in order to account for the miscalculation of errors on evidences known to happen in nested sampling algorithms (see Nelson et al. 2018); however, we note that in our case, given the large amount of data (especially given we have strong constraints on the ephemerides of at least one planet in this work from transit photometry), the empirically determined errors on the evidences (calculated by running each model run five times) are always $\ln Z < 1$ — typically on the order of 0.1.

### 3.3.1 Photometry-only analysis

For the analysis of the TOI-141 system, we first performed a photometry-only analysis with juliet in order to find constraints on the time of transit center and period of the orbit

**Table 3.** Priors used in our joint analysis of the TOI-141 system using `juliet` for the analysis of TOI-141b and TOI-141c. Our stellar density prior is the one derived in Section 3.1. Here $p = R_p/R_*$ and $b = (a/R_*)\cos(i_p)$, where $R_p$ is the planetary radius, $R_*$ the stellar radius, $a$ the semi-major axis of the orbit and $i_p$ the inclination of the planetary orbit with respect to the plane of the sky. $e$ and $\omega$ are the eccentricity and argument of periastron of the orbits. $\mathcal{N}(\mu, \sigma^2)$ represents a normal distribution of mean $\mu$ and variance $\sigma^2$. $\mathcal{U}(a, b)$ represents a uniform distribution between $a$ and $b$. $\mathcal{J}(a, b)$ represents a Jeffrey's prior (i.e., a log-uniform distribution) between $a$ and $b$.

| Parameter name | Prior | Units | Description |
|---|---|---|---|
| **Parameters for TOI-141** | | | |
| $\rho_*$ | $\mathcal{N}(1127, 33^2)$ | kg/m$^3$ | Stellar density of TOI-141. |
| **Parameters for TOI-141b** | | | |
| $P_b$ | $\mathcal{N}(1.0079, 0.0100^2)$ | days | Period of TOI-141b. |
| $t_{0,b}$ | $\mathcal{N}(2458379.9647, 0.0100^2)$ | days | Time of transit-center for TOI-141b. |
| $r_{1,b}$ | $\mathcal{U}(0, 1)$ | — | Parametrization[1] of Espinoza (2018) for $p$ and $b$ for TOI-141b |
| $r_{2,b}$ | $\mathcal{U}(0, 1)$ | — | Parametrization[1] of Espinoza (2018) for $p$ and $b$ for TOI-141b |
| $K_b$ | $\mathcal{U}(0, 100)$ | m/s | Radial-velocity semi-amplitude for TOI-141b. |
| $\mathcal{S}_{1,b} = \sqrt{e_b}\sin\omega_b$ | $\mathcal{U}(-1, 1)$ | — | Parametrization[2] for $e$ and $\omega$ for TOI-141b. |
| $\mathcal{S}_{2,b} = \sqrt{e_b}\cos\omega_b$ | $\mathcal{U}(-1, 1)$ | — | Parametrization[2] for $e$ and $\omega$ for TOI-141b. |
| **Parameters for TOI-141c** | | | |
| $P_c$ | $\mathcal{N}(4.75, 1.00^2)$ | days | Period of TOI-141c. |
| $t_{0,c}$ | $\mathcal{N}(2458397.00, 1.00^2)$ | days | Time of transit-center for TOI-141c. |
| $K_c$ | $\mathcal{U}(0, 100)$ | m/s | Radial-velocity semi-amplitude for TOI-141c. |
| $\mathcal{S}_{1,c} = \sqrt{e_c}\sin\omega_c$ | $\mathcal{U}(-1, 1)$ | — | Parametrization[2] for $e$ and $\omega$ TOI-141c. |
| $\mathcal{S}_{2,c} = \sqrt{e_c}\cos\omega_c$ | $\mathcal{U}(-1, 1)$ | — | Parametrization[2] for $e$ and $\omega$ TOI-141c. |
| **Parameters for TESS photometry** | | | |
| $D_{\mathrm{TESS}}$ | 1 (fixed) | — | Dilution factor for TESS. |
| $M_{\mathrm{TESS}}$ | $\mathcal{N}(0, 0.1^2)$ | relative flux | Relative flux offset for TESS. |
| $\sigma_{w,\mathrm{TESS}}$ | $\mathcal{J}(0.1, 5000^2)$ | relative flux (ppm) | Extra jitter term for TESS lightcurve. |
| $q_{1,\mathrm{TESS}}$ | $\mathcal{U}(0, 1)$ | — | Quadratic limb-darkening parametrization[3] (Kipping 2013). |
| $q_{2,\mathrm{TESS}}$ | $\mathcal{U}(0, 1)$ | — | Quadratic limb-darkening parametrization[3] (Kipping 2013). |
| **RV parameters** | | | |
| $\mu_{\mathrm{FEROS}}$ | $\mathcal{N}(36140, 30^2)$ | m/s | Systemic velocity for FEROS. |
| $\sigma_{w,\mathrm{FEROS}}$ | $\mathcal{J}(0.01, 30^2)$ | m/s | Extra jitter term for FEROS. |
| $\mu_{\mathrm{HARPS}}$ | $\mathcal{N}(36162, 30^2)$ | m/s | Systemic velocity for HARPS. |
| $\sigma_{w,\mathrm{HARPS}}$ | $\mathcal{J}(0.01, 30^2)$ | m/s | Extra jitter term for HARPS. |
| $\mu_{\mathrm{CORALIE07}}$ | $\mathcal{N}(36088, 30^2)$ | m/s | Systemic velocity for CORALIE07[4]. |
| $\sigma_{w,\mathrm{CORALIE07}}$ | $\mathcal{J}(0.01, 30^2)$ | m/s | Extra jitter term for CORALIE07[4]. |
| $\mu_{\mathrm{CORALIE14}}$ | $\mathcal{N}(36135, 30^2)$ | m/s | Systemic velocity for CORALIE14[4]. |
| $\sigma_{w,\mathrm{CORALIE14}}$ | $\mathcal{J}(0.01, 30^2)$ | m/s | Extra jitter term for CORALIE14[4] |

[1] To perform the transformation between the $(r_1, r_2)$ plane and the $(b, p)$ plane, we performed the transformations outlined in Espinoza (2018), which depend on $r_1$ and $r_2$, and a set of limits for the minimum and maximum $p$, $p_l$ and $p_u$, to consider: if $r_1 > A_r = (p_u - p_l)/(2 + p_l + p_u)$, then $(b, p) = ([1 + p_l][1 + (r_1 - 1)/(1 - A_r)], (1 - r_2)p_l + r_2 p_u)$. If $r_1 \leq A_r$, then $(b, p) = ([1 + p_l] + \sqrt{r_1/A_r}\, r_2(p_u - p_l), p_u + (p_l - p_u)\sqrt{r_1/A_r}[1 - r_2])$. In this work, we set $p_l = 0$ and $p_u = 1$.
[2] We ensure in each sampling iteration that $e = \mathcal{S}_1^2 + \mathcal{S}_2^2 \leq 1$.
[3] To transform from the $(q_1, q_2)$ plane to the plane of the quadratic limb-darkening coefficients, $(u_1, u_2)$, we use the transformations outlined in Kipping (2013) for this law $u_1 = 2\sqrt{q_1}q_2$ and $u_2 = \sqrt{q_1}(1 - 2q_2)$.
[4] CORALIE07 corresponds to data taken between the 2007 and 2014 upgrade and CORALIE14 corresponds to data taken after the 2014 upgrade (see Section 2.6).

of TOI-141.01 using the priors defined for the photometric elements in Table 3, which were based on our BLS search and the TESS alerts best period for this candidate. We consider the possibility that the TESS photometry might need a GP to account for any residual time-correlated noise in the lightcurve, and for this we fitted both a transit model plus an exponential-squared GP and a transit model assuming a white-noise model only. We found that both models were indistinguishable from one another based on their model evidences ($\Delta \ln Z < 1$), and thus decided to use the simpler model (i.e., a no-GP, white-noise model) when analyzing the PDC photometry. We note that for the white-noise model we add an extra photometric jitter term in quadrature to the reported uncertainties in order to account for miscalculations of the photometric uncertainties or any residual astrophysical signal not captured by our modelling.

In addition to this fit, we also tried a fit assuming there is an additional transiting planet in the system to TOI-141.01, with the same photometric priors as the ones used for this candidate presented in Table 3, except for the period and time of transit center; the first was left to freely vary between 0.1 and 14 days (for the same reason this were the trial periods in our BLS analysis in Section 2), whereas the second was left to vary from the time of the start of the observations to 15 days later. We found no evidence on the data for additional transiting planets ($\ln Z > 100$ in favor of the 1-planet model) in agreement with our results from the BLS search in Section 2.

### 3.3.2 RV-only analysis

We ran a `juliet` run on the radial velocities independently in order to see if we were able to find evidence for planets in the radial-velocity dataset alone. For this, we ran three models: (1) no planet (i.e., variation in the data solely explained by the jitters of the data, which were let to float as free parameters), (2) one planet in the RVs, (3) two planets in the RVs. We modelled the planetary signals using simple Keplerians assuming circular orbits with the same priors as the radial-velocity elements in Table 3. However, for this excercise we gave wide log-uniform priors for the period from 0.1 to 30 days for both planets (with the constraint that one planetary period is always larger than the other in order to avoid multiple modes for exchangable periods) and the times of transit center set with uniform priors between the start of the observations and 30 days later[6]. The limit of 30 days was set as our most constraining RV datasets (the FEROS and HARPS datasets) are only ∼ 60 days in total duration, and as such periods up to half this baseline are reasonable to search in the dataset.

The resulting evidences for the models strongly favor the 1 and 2-planet models in the data over the no-planet model. The 1-planet model converges to a posterior period of 4.75±0.01 days, and it has a log-evidence 56 times larger than the no-planet model, i.e., the 1-planet model is 24 orders of magnitude more likely than the null model. In turn, the two-planet model converges to both a period of $1.00940 \pm 0.00036$ days for one of the planets and of $4.7604 \pm 0.0028$ days for the other — this model in turn has a log-evidence 52 times larger than the 1-planet model, and 108 times larger than the no-planet model. We note how in this 2-planet model the smallest period is consistent with the period of the transit events observed by TESS, albeit with a small offset, most likely due to the sampling of the data (i.e., given a signal with a period equal to that of the transit ephemerides in our data, this offset is expected given the alias of 1-day the window function imprints on our radial-velocity measurements; see Dawson & Fabrycky 2010, for details, and our discussion below). This acts as an independant confirmation of the transit signal observed in the TESS photometry — we consider these observations thus confidently confirm

the transit signatures observed by TESS as a bona-fide exoplanetary signal, to which we refer to as TOI-141b in what follows.

The 4.8-day signal, although well-fitted with a Keplerian, could also be caused by stellar activity and not by the reflex motion of a planet around the star. We anticipate that this is not very likely, as the star's chromospheric emission as measured by the $\log R'_{\mathrm{HK}}$ has been actually measured before our observations to be quite low (−4.90 ± 0.05; Henry et al. 1996), which combined with its $B − V = 0.62$ color, would imply it resides in the region where inactive stars reside in the $B − V / \log R'_{\mathrm{HK}}$ diagram. On top of this, assuming the stellar axis is aligned with the plane of the sky, we can derive a rotation period of the (equator of the) star of 18.58 ± 1.28 days from the stellar radius and the $v \sin i_*$ value presented in Table 2, which is much too large to explain the evident 4.8-day variations observed in our radial velocities. Indeed, the periodogram of monitored external variables, such as Mount Wilson's S-index shows no clear peak around the periods of interest, and the same results are obtained for the bisector span (Figure 3). We nonetheless consider this possibility in the next sub-section when we perform the joint photometric and RV analysis.

### 3.3.3 Photometric and RV analysis

With the above defined information, we performed a joint analysis of the photometry and radial-velocity of TOI-141 using `juliet`, which we use to jointly constrain all the parameters of the orbits of both TOI-141b and the possible 4.75-day planetary signal in the TOI-141 system. We use normal priors for the periods and time of transit centers of those signals, with mean values taken from our photometry and radial-velocity only analyses, and with standard-deviations enlarged by a factor of a thousand with respect to those found in those analyses. All the other parameters are left to explore the whole parameter space of physically plausible ranges.

In order to study the nature of the 4.8-day signal found in our radial-velocity only analysis and any possible additional signals in the radial velocities, we performed two groups of joint analyses in which we explored (1) how strongly this extra signal is supported by the data, (2) what the nature of this extra signal is (i.e., planetary or stellar activity) and (3) if there is any evidence for additional signals on top of this extra signal in the radial velocities. To explore (1) and (2) we considered two possible models for this extra signal: a Keplerian or a GP. For the Keplerian model, we used the priors presented in Table 4. For the GP model, we used the same priors but instead of adding the parameters corresponding to planet c, we used a GP to account for the extra signal with three different possible kernels. The first was a squared-exponential kernel using either time, S-index or bisector spans as inputs, i.e., a kernel of the form

$$k_{i,j}(\tau) = \sigma_{\mathrm{GP}}^2 \exp\left(-\alpha_{\mathrm{GP}}\tau^2\right),$$

where $\tau = x_i - x_j$, is the lag between the mentioned state-variables (which were fed normalized — i.e., they were mean-substracted and divided by their standard-deviations), $\sigma_{\mathrm{GP}}$ is the amplitude of this GP component and $\alpha_{\mathrm{GP}}$ is the inverse length-scale of this parameter. The second kernel

---

[6] In practice, this gave rise to many local minima corresponding to integer times the period along the observations but this is not a problem for the nested sampling algorihtms used by `juliet`— see Espinoza et al. (2018) for details on this point.
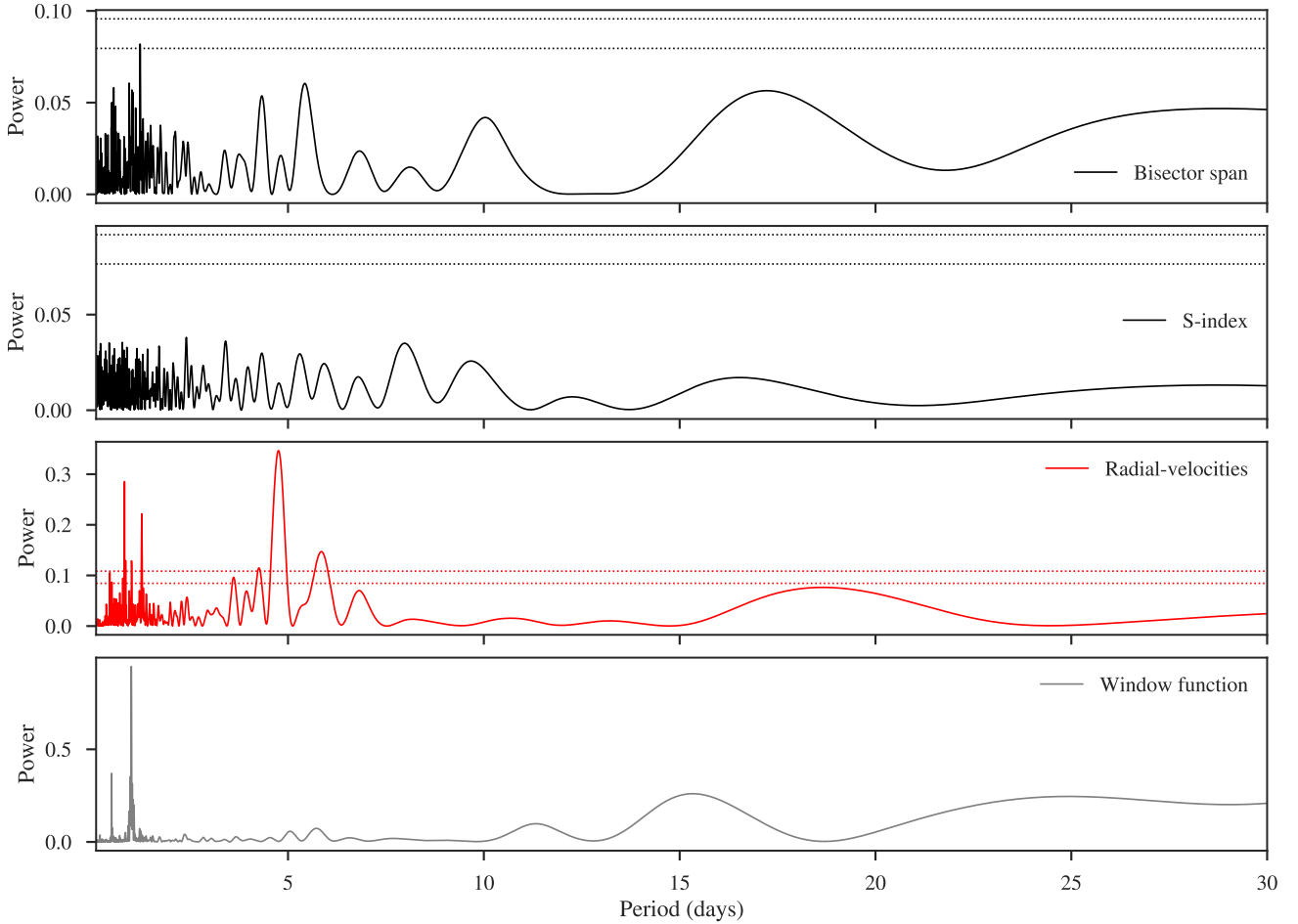
**Figure 3.** Generalized Periodogram for the bisector span (top), S-index (second panel), the radial velocities (third panel) and the window function (bottom). Dotted lines in each panel denote the 1% and 5% false-alarm probabilities. Periodograms calculated with the Generalized Lomb Scargle periodogram (Zechmeister & Kürster 2009) and with false-alarm probabilities calculated via bootstrapping with `astroML` (Vanderplas et al. 2012).

we explored was the quasi-periodic kernel introduced by Foreman-Mackey et al. (2017), which is of the form

$$k_{i,j}(\tau) = \frac{B}{2+C} e^{-\tau/L} \left[ \cos\left(\frac{2\pi\tau}{P_{\rm rot}}\right) + (1+C) \right]$$

and where $\tau = t_i - t_j$ is the time-lag. Here $B$ and $C$ are terms that normalize and amplify the kernel, whereas $L$ is an exponential decay time-scale and $P_{\rm rot}$ is the period of the quasi-periodic GP. Finally, we also explored the widely used exp-sine-squared kernel of the form

$$k_{i,j}(\tau) = \sigma_{\rm GP}^2 \exp\left(-\alpha_{\rm GP}\tau^2 - \Gamma \sin^2\left[\frac{\pi\tau}{P_{\rm rot}}\right]\right),$$

where $\tau = t_i - t_j$ is again the time-lag, $\sigma_{\rm GP}$ is the amplitude of the GP component, $\alpha_{\rm GP}$ is an inverse time-scale for the GP, $\Gamma$ is the amplitude of the periodic component of the GP and $P_{\rm rot}$ is, again, the period of the quasi-periodic component. The priors used for the hyper-parameters of those GP models are listed in Table 4.

The first four items in Table 5 show the results of this first group of fits performed on our data. As can be seen, among those models the best one given the data appears to be the one which includes one planet (the transiting one)

plus the kernel introduced by Foreman-Mackey et al. (2017). This result is interesting because the periodic component of the GP is clearly trying to fit for a 4.8-day periodic component plus some extra signal in the data in this case, which led us to believe that the best model could be one which has two Keplerians (one for the transiting planet and one for the 4.8-day signal) and an additional GP component on top of them (i.e., point (3) above). Motivated by this possibility, we performed a second group of fits with two Keplerians plus a GP, where we tried the same kernels as for the first group of fits (i.e., with the priors on the GP hyperparameters given in Table 4). The results of our fits for this second group of fits are also presented in Table 5 (three last items in the list).

As can be seen in Table 5, the models with the highest evidences are models with two planets and an additional GP component[7]. At face value, the model with the highest evidence is the one using the Foreman-Mackey et al.

---

[7] We also tried 3-planet fits, but these show much smaller log-evidences than the models presented here. A 3-planet fit with the third component having a log-prior on the period from 5 to 100

**Table 4.** Priors used for our fits including GPs. These were used in conjunction with the priors listed in Table 3.
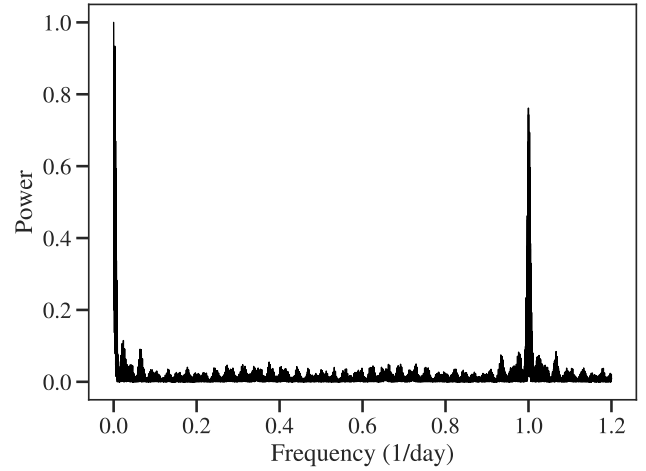
| Parameter name | Prior | Units | Description |
|---|---|---|---|
| Parameters for the squared exponential kernel | | | |
| $\sigma_{\rm GP}$ | $\mathcal{J}(10^{-5}, 1000)$ | m/s | Amplitude of GP component. |
| $\alpha_{\rm GP}$ | $\mathcal{J}(10^{-5}, 1000)$ | — | Inverse length-scale of the GP component. |
| Parameters for the quasi-periodic kernels | | | |
| $P_{\rm rot}$ | $\mathcal{N}(4.75, 1.00^2)$ | days | Period of the quasi-periodic component. |
| Parameters for (Foreman-Mackey et al. 2017) quasi-periodic kernel | | | |
| $B$ | $\mathcal{J}(10^{-5}, 1000)$ | m$^2$/s$^2$ | Amplitude of GP component. |
| $C$ | $\mathcal{J}(10^{-5}, 1000)$ | — | Factor of GP component. |
| $L$ | $\mathcal{J}(10^{-5}, 1000)$ | 1/day | Lengthscale of the quasi-periodic component. |
| Parameters for the exp-sine-squared GP | | | |
| $\sigma_{\rm GP}$ | $\mathcal{J}(10^{-5}, 1000)$ | m/s | Amplitude of GP component. |
| $\alpha_{\rm GP}$ | $\mathcal{J}(10^{-5}, 1000)$ | — | Inverse length-scale of the GP component. |
| $\Gamma$ | $\mathcal{J}(10^{-5}, 1000)$ | — | Amplitude of the sine-squared term in the GP. |

**Table 5.** Resulting log-evidences (and differences with respect to the model selected as the "best" model — in bold) from different model fits to the full photometric and RV datasets with the priors defined in Tables 3 and 4 (see text). SE stands for results using a squared-exponential kernel, whereas FM stands for results using the Foreman-Mackey et al. (2017) quasi-periodic kernel. The value presented for the 1 planet + SE GP below corresponds to the model using time as a variable, which was the model that gave the best fit among that class of models. The 2 planet + SE GP model was selected as the best model as is indistinguishable between the other 2-planet GP fits ($|\Delta \ln Z < 1|$), and is the simpler (i.e., has lower number of free parameters) of them.

| Model | $\ln Z$ | $\Delta \ln Z$ |
|---|---|---|
| 2 planets | 111,484.42 | -49.0 |
| 1 planet + SE GP | 111,505.87 | -27.5 |
| 1 planet + exp-sine-squared QP GP | 111,516.60 | -16.8 |
| 1 planet + FM QP GP | 111,526.35 | -7.07 |
| 2 planets + exp-sine-squared QP GP | 111,533.07 | -0.35 |
| **2 planets + SE GP** | **111,533.42** | **0** |
| 2 planets + FM QP GP | 111,533.61 | 0.19 |



**Figure 4.** Window function of our radial-velocity samples. Two peaks emerge in the window shown here, one at 0.001 day$^{-1}$ and another one at 1.00185 day$^{-1}$.

(2017) quasi-periodic kernel, but this model is in practice indistinguishable ($|\Delta \ln Z < 1|$) from both a fit using an exp-sine-squared kernel and a squared-exponential kernel. Interestingly, the quasi-periodic kernels in these 2-planet fits actually provide no constraint on the extra residual periodic component — the posterior on the $P_{\rm rot}$ parameters only rules out periods smaller than about 5-days, and is uniform in the rest of the parameter space, which hints that the presence of any additional periodic signal (e.g., activity and/or extra planetary companions) is unlikely given our data. In fact, all three fits converge to the same posterior parameters for all the orbital and physical parameters of the planets in the system. Being the 2-planet plus squared-exponential GP the simpler of the mentioned fits, we choose this as our best model in this case; this model is in turn superior to both the 1-planet models assuming an extra squared-exponential kernel or a quasi-periodic kernel and to the 2-planet fit without

gives a log-evidence worse than the best model presented in this work.

a GP component. Together with our discussion in the previous section that stellar activity indicators show no evident peaks in the periodogram at the periods of interest, and that the rotation period of the star is much longer than the period of interest, we take this as evidence that the observed signal is indeed caused by a non-transiting planet, to which we refer from now on to as TOI-141c. It is interesting to note that our posterior distribution for the period of planet TOI-141c is actually multi-modal with the two main periods being at $4.75983^{+0.00046}_{-0.00043}$ days and at $4.78503^{+0.00056}_{-0.00051}$ days. It is under this latter period that most of the posterior density is located, in fact. However, an additional piece of evidence that this latter one is the true period of TOI-141c comes from examining our window function (Figure 4). The function shows the expected peak around the solar day (1.0018 day$^{-1}$ in our window function), which in turn is propagated also to lower and higher frequencies. In particular, the largest peak in our window function in frequency space is at $f_{\rm s} = 0.001$ day$^{-1}$. Given a real frequency present in the data, thus, aliases of this frequency will emerge at $f_{\rm alias} = f_{\rm true} \pm m f_{\rm s}$, where $m$ is an integer, $f_{\rm true}$ is the true, underlying frequency embed-

ded in the dataset, $f_{alias}$ is the generated alias and $f_s$ is a peak from the window function. Indeed, if the 4.78503 period is the real period, then with $f_s = 0.001$ day$^{-1}$ this signal should generate aliasing signals at periods of 4.76 and 4.81 days, both of which we do see in our posterior distribution for the period. If the real period were 4.75983 days, on the other hand, this should give rise to aliasing signals at periods of 4.78 and 4.73 days — the latter not being present in our posterior distribution. To make a quantitative assessment of this, we used the `AliasFinder` package (Stock & Kemmer, in prep.)[8], which implements the procedure for alias finding detailed in Dawson & Fabrycky (2010). Using this tool with both of these periods yields the same suggestion: that the 4.78503 period is the real period, with the 4.75983 period being an alias. Because of this, the period of $4.78503^{+0.00056}_{-0.00051}$ days is the one we report as our final estimate for the period of this exoplanet. We note that there is no strong correlation between the period and any other parameter in Figure 5 — this multi-modal nature, however, appears not only on our GP fits but also on our 2-planet white-noise fits, which suggests that, indeed, these appear because of the sampling of the data. Importantly, this bi-modal nature of this period, does not enlarge the uncertainties in the other retrieved parameters.

The posterior distribution of the parameters of our best-fit model are presented in Table 6 for all the parameters except for the eccentricities and the jitter terms mentioned above — for those parameters we present upper limits based on the fits performed allowing those to vary freely in our `juliet` runs; the corresponding posterior modelling of the data is presented in Figure 6 for the photometry and Figure 7 for the radial velocities. A close-up to the radial velocities showing how each component of our model adds to the full signal is presented in Figure 8.

As can be observed in Figure 8 and from the derived inverse length-scale reported in Table 6, the GP-component tries to explain a stochastic variation with a typical time-scale $(1/\sqrt{2\alpha_{GP}})$ of $\sim 3$ hours with an amplitude of about $\sim 2$ m/s. It is unlikely this is some kind of stellar oscillation, as the amplitude of them in radial velocities of stars similar to the Sun like TOI-141 are about one order of magnitude smaller and occur at scales of minutes and not of hours (see, e.g., Carrier & Bourban 2003; Elsworth & Thompson 2004). One possibility is that our GP component is modelling instrumental systematics; these could be coming mainly from the FEROS dataset, which is the dominant source of RVs in our work, for which stability at the precision level attained in this work ($\sim 2$ m/s) has not been tested so far at such timescales.

The derived physical parameters presented in Table 6 for the transiting exoplanet TOI-141b present a remarkable similarity with the benchmark exoplanet 55 Cancri e (a.k.a. Janssen, Fischer et al. 2008; Winn et al. 2011). According to the latest analysis of this latter transiting exoplanet by Bourrier et al. (2018), 55 Cancri e has a radius of $R_P = 1.88 \pm 0.03 R_\oplus$ and mass of $M_P = 8.0 \pm 0.3 M_\oplus$, which implies a density of $\rho_P = 6.7 \pm 0.4$ g cm$^{-3}$. Similarly TOI-141b has a radius of $R_P = 1.745^{+0.051}_{-0.052} R_\oplus$ and mass of $M_P = 8.83^{+0.66}_{-0.65} M_\oplus$, which in turn implies a (larger, but still consis-

[8] https://github.com/JonasKemmer/AliasFinder

**Table 6.** Posterior parameters obtained from our `juliet` analysis for TOI-141b and TOI-141c

| Parameter name | Posterior estimate[a] |
|---|---|
| **Posterior parameters for TOI-141b** | |
| $P_b$ (days) | $1.008035^{+0.000021}_{-0.000020}$ |
| $t_{0,b}$ (BJD UTC) | $2458379.97043^{+0.0012}_{-0.0012}$ |
| $\rho_*$ (kg/m$^3$) | $1127.4^{+31.8}_{-31.3}$ |
| $r_{1,b}$ | $0.783^{+0.022}_{-0.027}$ |
| $r_{2,b}$ | $0.01453^{+0.00041}_{-0.00042}$ |
| $K_b$ (m/s) | $5.30^{+0.39}_{-0.39}$ |
| $e_b$ | 0 (fixed[b], < 0.24) |
| **Posterior parameters for TOI-141c** | |
| $P_c$ (days) | $4.78503^{+0.00056}_{-0.00051}$ |
| $t_{0,c}$ (BJD UTC) | $2458396.635^{+0.054}_{-0.054}$ |
| $K_c$ (m/s) | $7.26^{+0.48}_{-0.47}$ |
| $e_c$ | 0 (fixed[b], < 0.16) |
| **Posterior parameters for TESS photometry** | |
| $M_{TESS}$ (ppm) | $-21^{+2.2}_{-2.2}$ |
| $\sigma_{w,TESS}$ (ppm) | $111.1^{+4.0}_{-4.0}$ |
| $q_{1,TESS}$ | $0.23^{+0.31}_{-0.17}$ |
| $q_{2,TESS}$ | $0.43^{+0.35}_{-0.29}$ |
| **Posterior RV parameters** | |
| $\mu_{FEROS}$ (m/s) | $36131.07^{+0.40}_{-0.40}$ |
| $\sigma_{w,FEROS}$ (m/s) | $0.88^{+0.82}_{-0.81}$ |
| $\mu_{HARPS}$ (m/s) | $36159.65^{+0.53}_{-0.53}$ |
| $\sigma_{w,HARPS}$ (m/s) | 0 (fixed[b], < 2.16) |
| $\mu_{CORALIE07}$ (m/s) | $36088.8^{+1.8}_{-1.8}$ |
| $\sigma_{w,CORALIE07}$ (m/s) | 0 (fixed[b], < 8.68) |
| $\mu_{CORALIE14}$ (m/s) | $36133.1^{+1.4}_{-1.5}$ |
| $\sigma_{w,CORALIE14}$ (m/s) | 0 (fixed[b], < 2.51) |
| $\sigma_{GP}$ (m/s) | $2.08^{+0.32}_{-0.29}$ |
| $\alpha_{GP}$ (1/day$^2$) | $27.1^{+27.0}_{-17.2}$ |
| **Derived transit parameters for TOI-141b** | |
| $R_P/R_*$ | $0.01453^{+0.00041}_{-0.00042}$ |
| $b = (a/R_*)\cos(i_P)$ | $0.675^{+0.033}_{-0.041}$ |
| $a_b/R_*$ | $3.927^{+0.037}_{-0.037}$ |
| $i_P$ (deg) | $80.09^{+0.62}_{-0.50}$ |
| $u_1$ | $0.34^{+0.34}_{-0.23}$ |
| $u_2$ | $0.063^{+0.35}_{-0.27}$ |
| **Derived physical parameters for TOI-141b** | |
| $M_P$ ($M_\oplus$) | $8.83^{+0.66}_{-0.65}$ |
| $R_P$ ($R_\oplus$) | $1.745^{+0.051}_{-0.052}$ |
| $\rho_P$ (g cm$^{-3}$) | $9.15^{+1.1}_{-1.0}$ |
| $g_P$ (m s$^{-2}$) | $28.5^{+2.8}_{-2.7}$ |
| $a$ (AU) | $0.02012^{+0.00015}_{-0.00012}$ |
| $T_{eq}$ (K)[c] | $2128^{+13}_{-14}$ |
| **Derived physical parameters for TOI-141c** | |
| $M_P \sin(i_P)$ ($M_\oplus$) | $19.95^{+1.38}_{-1.36}$ |
| $a$ (AU) | $0.056798^{+0.00044}_{-0.00032}$ |
| $T_{eq}$ (K)[c] | $1265.4^{+7.3}_{-8.4}$ |

[a] Errorbars denote the 68% posterior credibility intervals (CI).
[b] Limits denote the 95% upper CI of fits allowing all orbits to be eccentric.
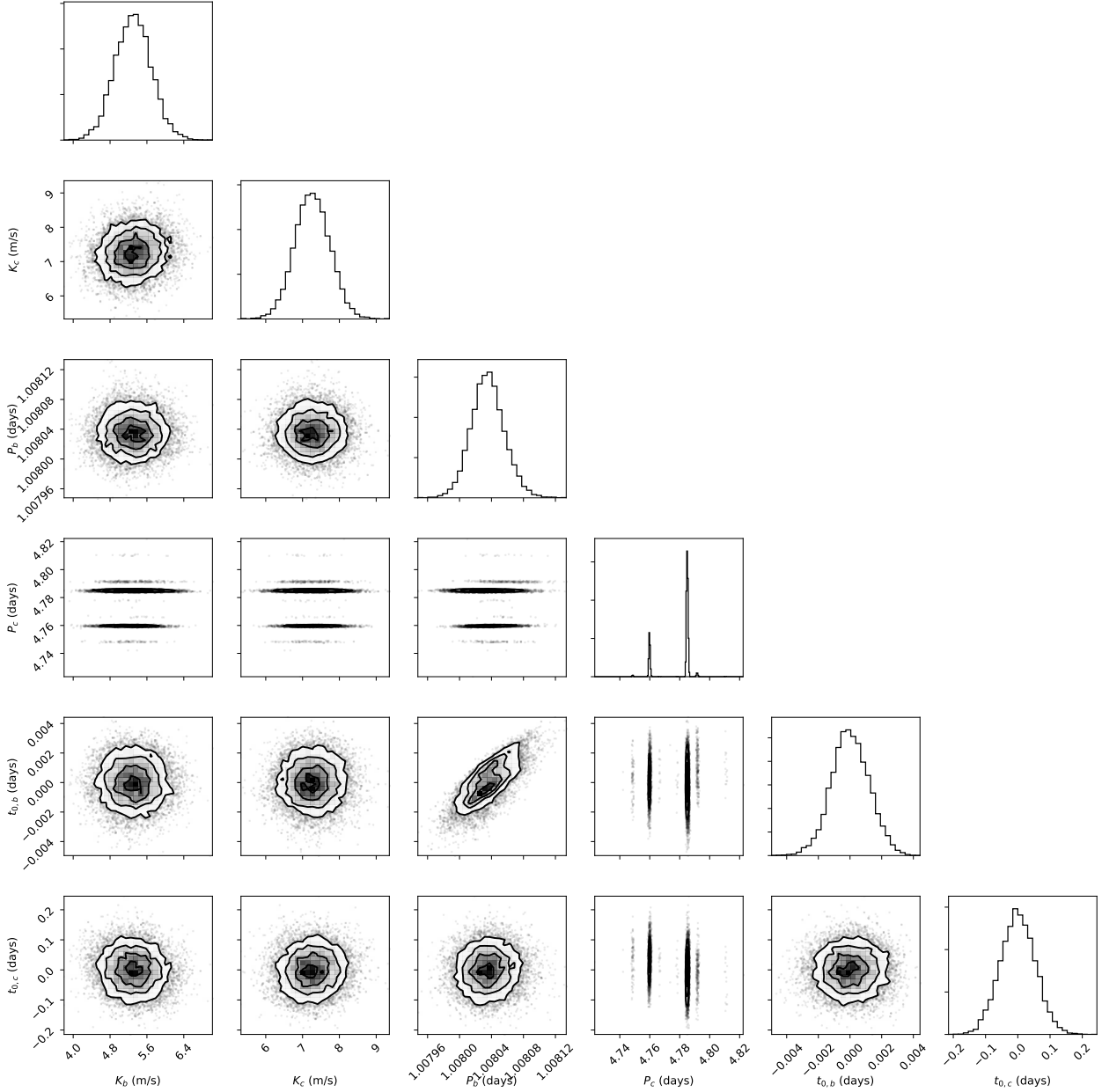[c] Equilibrium temperatures calculated assuming 0 Bond Albedo.

**Figure 5.** Corner plot of the posterior distribution of the main parameters of planet b and c, where the multi-modality of the period of planet $c$ is evident. The two main peaks of this multi-modal distribution are located at $4.75983^{+0.00046}_{-0.00043}$ days and at $4.78503^{+0.00056}_{-0.00051}$ days. We note that for the time-of-transit centers, the plotted values are the median-substracted values of the posteriors. This has been substracted for clarity in the corner plot.

tent at 2-sigma) density of $9.15^{+1.1}_{-1.0}$g cm$^{-3}$. Both exoplanets, thus, have statistically indistinguishable masses and radii (TOI-141b is only $\Delta R_p = 0.135 \pm 0.06 R_\oplus$ smaller than 55 Cancri e, i.e., consistent with 0 within $\sim 2$ standard deviations). In fact, this also applies to their irradiation levels as well: the zero-albedo equilibrium temperature of TOI-141b is only slightly higher than that of 55 Cancri e (only $\Delta T_{\rm eq} \approx 200$ K hotter than 55 Cancri e). Thus, TOI-141b can be thought of as a very similar exoplanet to 55 Cancri e, making it almost an analogue in terms of the planetary properties, given the current data at hand. We discuss the prospects that TOI-141b provides for planetary characterization and compara-

tive exoplanetology of transiting super-Earth exoplanets in light of this similarity in the next section.

The derived properties for TOI-141c are exciting as well. The minimum mass for TOI-141c of $M_P \sin(i_P) = 19.95^{+1.38}_{-1.36} M_\oplus$ suggests a minimum mass on the order of that of Neptune. Given the transiting nature of TOI-141b, we thus expect the inclination of this exoplanet to be not much larger than its inner companion, implying a true mass of the same order as the one implied by its minimum mass in our analysis.
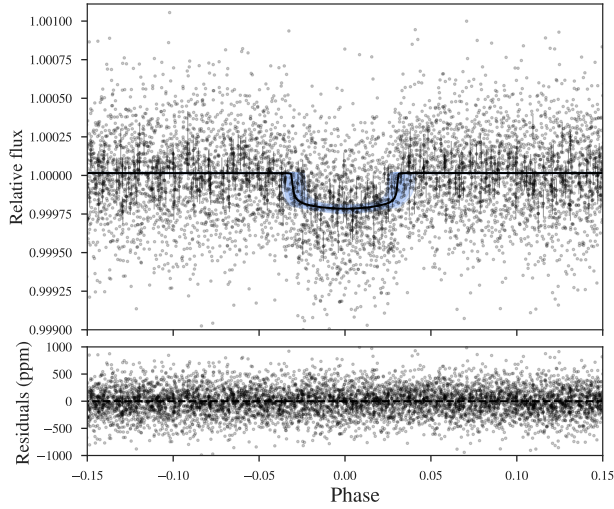
**Figure 6.** *Top.* TESS photometry phased around the period of TOI-141b (grey points; black points with errorbars correspond to 10-point binned photometry shown for illustration). The black line shows the median posterior model given the data, and blue bands denote its 68%, 95% and 99% posterior credibility bands. *Bottom.* Residuals obtained by substracting the data with our median posterior model.

### 3.4 Searching for transits of TOI-141c

We used the TESS photometry to search for transits of TOI-141c. For this, we performed a `juliet` run with the same priors as the ones defined in Table 3 for TOI-141c. We assumed a circular orbit for both exoplanets (as per our result in Section 3.3) and we added $r_{1,c}$ and $r_{2,c}$ as free parameters to TOI-141c with the same priors as the corresponding parameters for TOI-141b to allow a transiting scenario for TOI-141c. The resulting `juliet` runs with and without a transiting TOI-141c with this parametrization significantly favored the non-transiting model ($\ln Z = 5.4$ in favor of this model). Figure 9 shows the posterior distribution of the impact parameter $b_c = (a_c/R_*)\cos(i_{p,c})$ (where $a_c$ is the semi-major axis of planet $c$ and $i_{p,c}$ is the inclination of planet $c$) and the planet-to-star radius ratio of the planet, $p_c = R_{p,c}/R_*$, in the case of the joint fit assuming TOI-141c transits. The marginal distribution of the planet-to-star radius ratio implies that even if the planet were to transit, about 95% of the posterior density is bounded to be $p_c < 0.014$, i.e., a planetary radius $R_{p,c} < 1.7R_\oplus$. At the same time, in this transiting scenario the impact parameter, coupled with the tight constraint on the stellar density (and hence, on $a_c/R_*$) would imply that 95% of the posterior density of the inclination is above $i_{p_c} > 84.82$, implying $\sin(i_{p_c}) > 0.996$, and hence making the true mass $19.95^{+1.38}_{-1.36}M_\oplus < M_p < 20.05^{+1.36}_{-1.39}M_\oplus$. This would in turn give rise to a density for TOI-141c about two-times that of TOI-141b, which would imply an extremely dense object. The rareness of such an object thus adds to the statistical evidence that TOI-141c most likely does not transit TOI-141.

### 3.5 Secondary eclipses, phase-curve modulations, TTVs

A search for secondary eclipses and phase-curve modulations of either TOI-141b or TOI-141c turned out to be null in the TESS photometry. This is not surprising as both reflected and emitted light in the TESS bandpass for these exoplanets is expected to be quite low; on the order of a couple of ppm for TOI-141b and a couple tens of ppm for TOI-141c depending on its size.

In addition, we performed a search for transit timing variations (TTVs) on the transits of TOI-141b. For this, we used the posterior transit parameters presented in Table 6 as priors for transit fits to the individual transits with `juliet` where the time-of-transit center was left as a free parameter with a uniform prior between 2 hours before and 2 hours after of the expected time of transit center. The resulting measured TTVs are presented in Figure 10. As can be seen, there are no evident TTVs, except for the 12th transit observed by *TESS*, which appears to be half an hour later than expected. However, inspecting this portion of the lightcurve there is an evident decrease of flux during egress, most likely arising from instrumental effects, which is what produces this significant shift in the time of transit. With our observations, we can put an upper limit of about 2 minutes over a course of 27 days to any TTVs impacting the time-of-transit centers of TOI-141b. This was expected at least for TTVs generated by TOI-141c on TOI-141b, for which an order-of-magnitude estimate gives a TTV amplitude on the order of 4 seconds (Holman & Murray 2005).

## 4 DISCUSSION

### 4.1 The TOI-141 system

The TOI-141 system composed of TOI-141b and TOI-141c is a very interesting system. On the one hand, TOI-141b, as will be shown below in Section 4.2, is a bona-fide "super-Earth", i.e., a rocky planet significantly larger than our home planet. Figure 11 compares TOI-141b in particular in the mass-radius diagram of exoplanets smaller than 2 Earth-radii (retrieved from `exoplanets.org`) whose masses and radius are characterized at better than 20%. We plot the two-layer models of Zeng et al. (2016) for illustration.

As can be seen from Figure 11, TOI-141b appears to have a composition similar to that of the Earth according to two-layer models. In fact, among super-Earths, it appears this is one of the few exoplanets for which we can confidently claim this is the case, making it a very interesting exoplanet. This possibility will be discussed in detail in Section 4.2.

TOI-141c, on the other hand, is most likely a short-period Neptune if the mutual inclination with TOI-141b is not too large. We showed that given the data the most plausible scenario for TOI-141c is that it does not transit the star, and thus the maximum inclination of this planet with respect of the plane of the sky would be of $i_c < \arccos(a/R_*)^{-1}$, or $i_c < 84.829 \pm 0.051$ degrees. This in turn implies that the true mass of TOI-141c is most likely $M_{p,c} > 18.54 \pm 0.85M_\oplus$. We are not able to put any constraints on the mutual inclination between TOI-141b and TOI-141c other than this upper limit for TOI-141c.
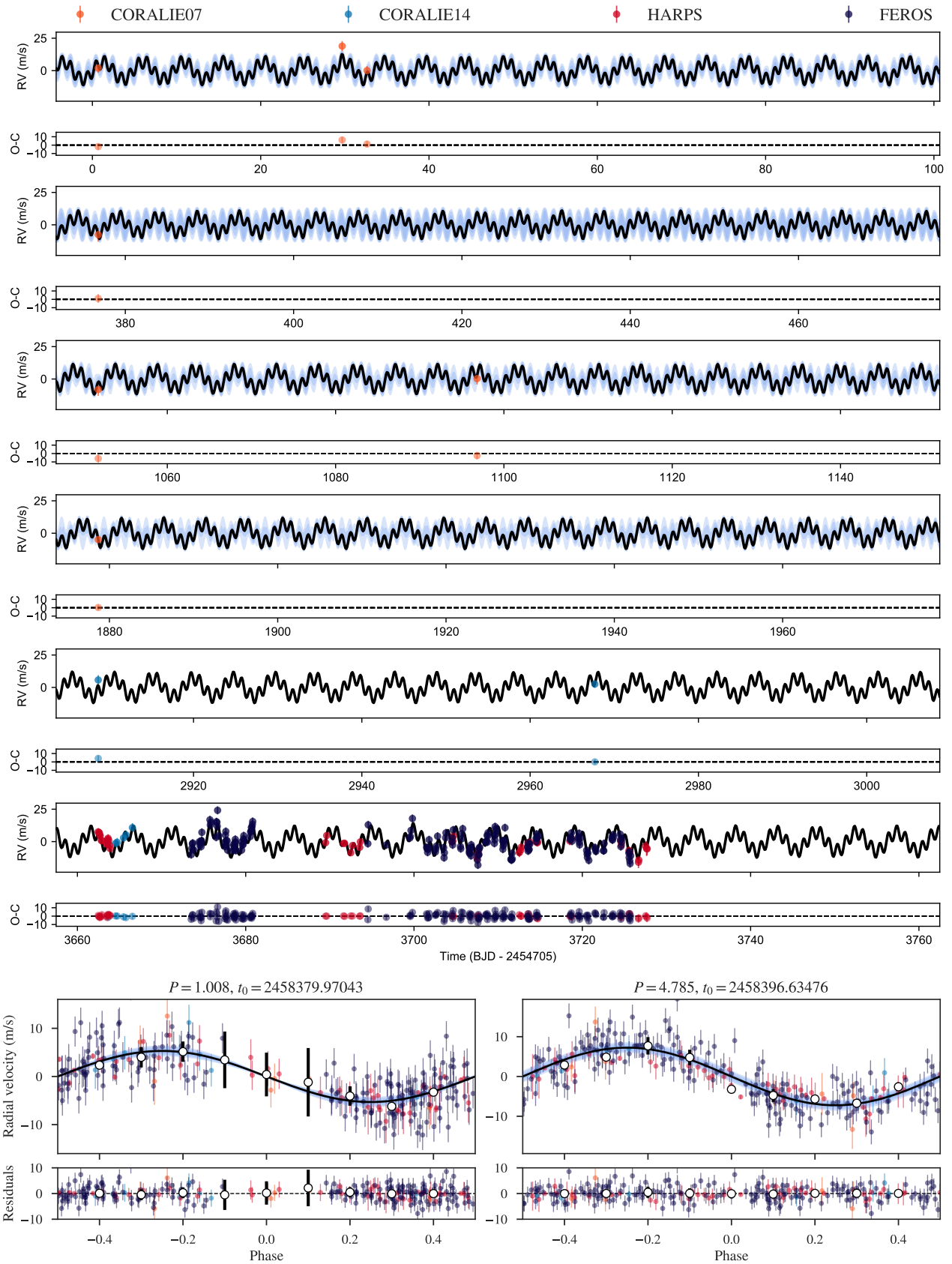
**Figure 7.** Systemic velocity-substracted radial velocities for the TOI-141 system observed by our FEROS (dark blue), HARPS (red) and CORALIE (orange and light blue) observations. The top panel shows the radial velocities as a function of time along with the residuals (O-C) obtained from substracting those with our median posterior model given the data (black lines; blue bands around it denoting 68%, 95% and 99% posterior credibility bands). Note the effects of the sampling of the inner, 1-day period planet, which made us sample almost identical phases on consecutive days. The bottom panel shows the phased radial velocities of TOI-141b (bottom left panel) and TOI-141c (bottom right panel) with the GP component removed, along with the phased residuals — white points show binned datapoints in phase for visualization. The same coloring as for the top panels is used for the bottom panels.
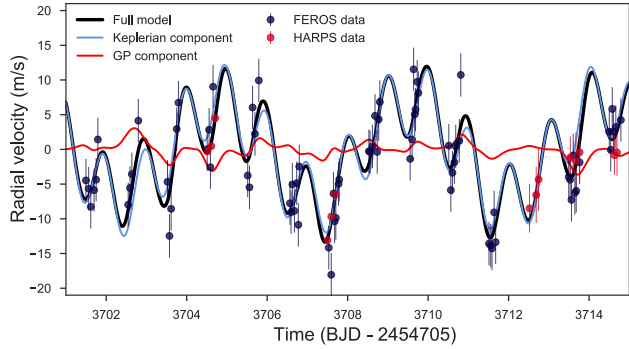
**Figure 8.** Close-up to the radial-velocity dataset presented in Figure 7, where we show each component of our best-fit model (black line): the keplerian (blue line) and the GP (red line) component.
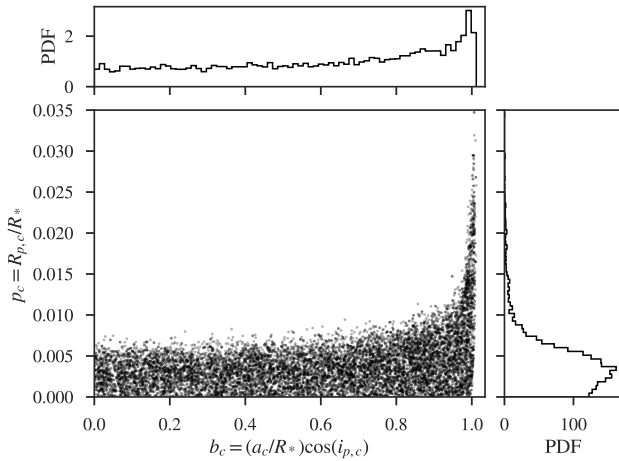


**Figure 9.** Posterior distribution of the impact parameter ($b_c$) and the planet-to-star radius ratio ($p_c$) for TOI-141c given the TESS photometry (central panel). The upper and right-side panels show the marginal distributions of each of those parameters.
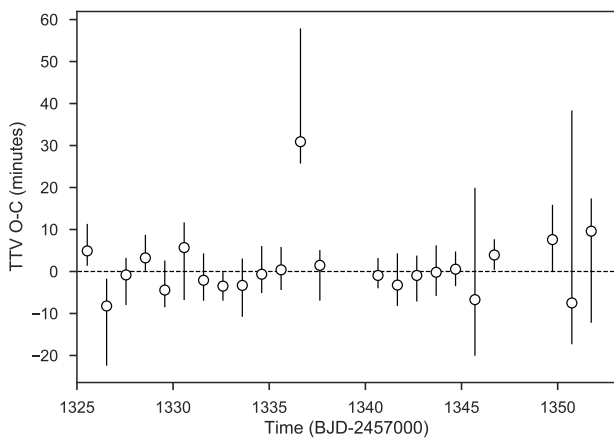


**Figure 10.** Transit timing variations (TTVs) for TOI-141b (i.e., observed minus expected time of transit center as a function of time). No evident variation is observed, putting a limit of ∼ 2 minutes to any TTV for TOI-141b.
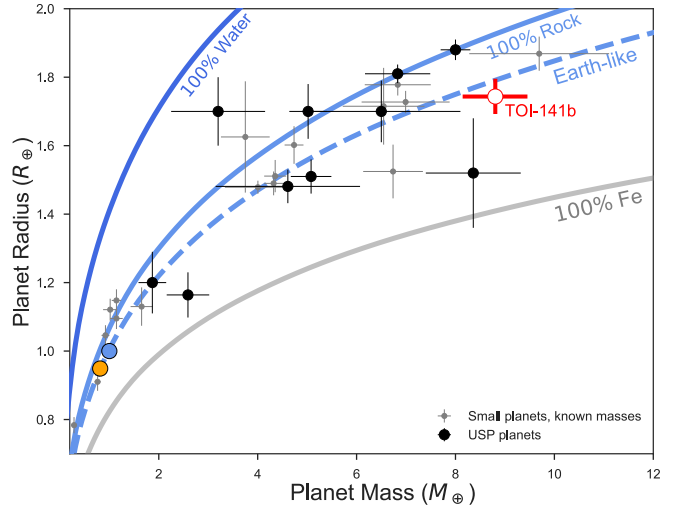


**Figure 11.** Mass/radius diagram for known exoplanets with sizes smaller than 2 Earth-radii. Black points identify USPs; TOI-141b is identified in red. Two-layer models are from Zeng et al. (2016); "Earth-like" here means a composition of 30% Fe and 70% $MgSiO_3$, whereas "100 % Rock" means a composition of 100% $MgSiO_3$. Earth is identified in this plot as a pale blue circle; the orange circle is Venus.

### 4.2 Interior composition of TOI-141b

#### 4.2.1 Interior characterization: method

For a detailed interior characterization, we use the probabilistic analysis of Dorn et al. (2017) which calculates possible interiors given the observed data (e.g., mass and radius as shown in Figure 11). Besides the data of mass and radius, we are using constraints on the possible bulk composition in terms of refractory elements (e.g., Fe, Mg, Si), which helps to refine interior predictions (Dorn et al. 2015). A proxy for the planet bulk composition is usually taken from the host star's photosphere. Here, measured stellar abundances of TOI-141b are (see Section 3.2) [Fe/H] = −0.04± 0.03, [Mg/H] = −0.04± 0.06, and [Si/H] = −0.03± 0.09. Thus, relative stellar abundances of Fe/Si and Mg/Si are similar to the Sun. In brief, our data comprise:

- Planet masses and radii (Table 6).
- Planet effective temperature (Table 6).
- Relative stellar abundances of Fe, Si and Mg of the host star.

Our assumptions for the interior model are similar to those in Dorn et al. (2017), but we consider a purely rocky planet. We assume an iron core and a silicate mantle, thus $r_{core+mantle}$ equals $R_p$. The interior parameters are core size $r_{core}$ and mantle composition (i.e., $Fe/Si_{mantle}$, $Mg/Si_{mantle}$). The prior distributions of the interior parameters are stated in Table 7.

Our interior model uses a self-consistent thermodynamic model from Dorn et al. (2017). For any given set of interior parameters, it allows us to calculate the respective mass, radius, and bulk abundances and compare them to the actual observed data. The thermodynamic model comprises the equation of state (EoS) of iron by Bouchet et al. (2013), the silicate-mantle model by Connolly (2009) to com-

**Table 7.** Prior ranges for interior parameters.

| Parameter | Prior range | Distribution |
|---|---|---|
| Core radius $r_{core}$ | $(0.01 - 1)\, r_{core+mantle}$ | uniform in $r_{core}^3$ |
| $Fe/Si_{mantle}$ | $0 - Fe/Si_{star}$ | uniform |
| $Mg/Si_{mantle}$ | $Mg/Si_{star}$ | Gaussian |

pute equilibrium mineralogy and density profiles given the database of Stixrude & Lithgow-Bertelloni (2011). We assume an adiabatic temperature profile within core and mantle.

### 4.2.2 Interior characterization: results and discussion

Figure 12 and Table 8 summarize posterior distributions of inferred interior parameters. Given bulk density, the planet is dominated by its rocky interior and might host a very thin terrestrial-type atmosphere only. The data of mass, radius, and bulk abundances inform possible core sizes and mantle compositions. Interestingly, the bulk abundance constraints cannot be reconciled with the measured bulk density of $\rho_p = 1.66\rho_\oplus$. This is because the abundance constraint favours Earth-like densities, while TOI-141b's bulk density is higher (see Figure 11). In order to better fit the bulk density, we relaxed the constraint on Fe/Si in a separate scenario and thereby allowed for rocky interiors with larger core mass fractions (Table 8). Although this scenario can well fit mass and radius, it remains unclear how such iron-rich interiors for massive super-Earths can be formed. The result of a possible iron-rich interior has to be discussed in light of our model assumptions and model uncertainties. Here, we have assumed pure iron cores for simplicity. The addition of light elements (e.g., O, Si, S, C) in the core can allow for larger cores and thus higher bulk densities, while fitting the measured bulk density. This suggests that the amount of light elements in the core can be constrained by mass, radius, and bulk abundances. Further investigations are underway to understand the importance of light core elements for super-Earths.

Here, we have chosen a rocky interior *a priori* and excluded atmospheres to significantly contribute to the planetary radius. We included possible terrestrial-like atmospheres in test runs that showed that possible atmosphere thicknesses are only tiny (0.01 $R_p$). Such thin atmospheres cannot be of primordial H/He, since atmospheric escape can efficiently erode thin H/He layer on short time-scales. An atmosphere of H/He is only stable against evaporative loss if it would be significantly thicker than the theoretical minimum threshold-thickness (Dorn & Heng 2018), which is 0.18 $R_p$ for TOI-141b. The threshold-thickness corresponds to the amount of gas ($H_2$) that is lost on short time-scale (here we use 100 Myr).

If this planet has indeed an atmosphere that can be characterized by spectroscopy, this planet would be an interesting target for investigating whether the atmosphere's origin can be informed by the chemical make-up and the extent of the atmosphere. Terrestrial-type atmospheres can be built during the outgassing of a cooling magma ocean or by

volcanism during the long-term evolution of a planet. The rate of volcanism can be very different depending on the convection regime of a planet, e.g., stagnant-lid versus plate tectonics (Kite et al. 2009). If TOI-141b is in stagnant-lid regime, no massive terrestrial-like atmosphere is expected since outgassing rates are very limited for $\gtrsim 8$ $M_\oplus$ planets (Dorn et al. 2018) despite its partly unconstrained interior structure and composition. A massive atmosphere of volcanic origin could only be present if the planet is in a different convection than stagnant-lid, e.g., plate tectonics. From the variety of modelling studies (Valencia et al. 2007; Kite et al. 2009; Noack & Breuer 2014; Korenaga 2010; Van Heck & Tackley 2011) however, it remains unclear whether Super-Earths can drive plate tectonics or not.

### 4.3 Atmospheric characterization of TOI-141b

Along with Kepler-10b (Batalha et al. 2011), Kepler-78b (Sanchis-Ojeda et al. 2013), K2-141b (Malavolta et al. 2018) and 55 Cancri e, TOI-141b joins the select group of rocky exoplanets that might be optimal targets for further atmospheric characterization with current and upcoming facilities. Given TOI-141b is so similar to 55 Cancri e, an exoplanet that has received particular attention in this front in recent years (see, e.g., Demory et al. 2016; Tsiaras et al. 2016; Angelo & Hu 2017; Miguel 2019), it is important to briefly discuss the prospects for atmospheric characterization of this newly discovered exoplanet. Among all the USPs, TOI-141b is the brightest one after 55 Cancri e. However, it is 2.4 magnitudes fainter in $K_s$ band and 2 magnitudes fainter in $V$ band than the latter. As such, this implies that characterizing the atmosphere of TOI-141b will be more challenging than the one performed so far for 55 Cancri e with known space telescopes such as *Spitzer* and *Hubble*. However, the fact that this provides one of the first exoplanets to perform a direct comparison to the observational properties of 55 Cancri e, makes this challenge a particularly interesting one to take. For the detection of the thermal emission for TOI-141b with *Spitzer*, this might involve over 10 transits to detect an occultation at 3-sigma confidence. As for transmission, the fainter nature of TOI-141b might actually help if observations are to be carried out with *Hubble*. For 55 Cancri e, spatial scans which left larger trails than usual were used in order to compute a transmission spectrum with HST/WFC3 (see discussion in Tsiaras et al. 2016). It is possible that this led to precisions 5 to 20% larger than the photon noise, whereas it is known that *Hubble* observations can achieve precisions close to 5% the photon-noise for bright stars (Knutson et al. 2014) — and thus this precision could be achieved for TOI-141b with *Hubble*. As such, TOI-141b
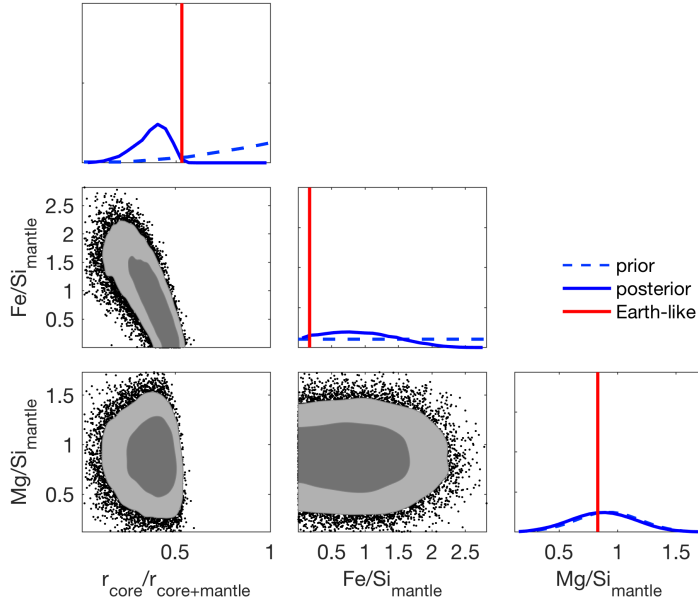
**Figure 12.** Two-and one-dimensional marginalised posteriors of interior parameters: core size ($r_{core}$), and mantle composition (Fe/Si$_{mantle}$ and Mg/Si$_{mantle}$). The prior distribution is shown in dashed, while the posterior distribution is shown in solid lines. An Earth-like interior is shown for reference.

**Table 8.** Interior parameter estimates. One-$\sigma$ uncertainties of the 1-D marginalized posteriors are listed.

| interior parameter | all constraints | no Fe/Si constraint | Earth-like value |
|---|---|---|---|
| $r_{core}/r_{core+mantle}$ | $0.38^{+0.07}_{-0.11}$ | $0.41^{+0.10}_{-0.12}$ | 0.53 |
| Fe/Si$_{mantle}$ | $0.87^{+0.60}_{-0.54}$ | $1.51^{+1.46}_{-0.98}$ | 0.17 |
| Mg/Si$_{mantle}$ | $0.87^{+0.26}_{-0.25}$ | $0.91^{+0.25}_{-0.25}$ | 0.83 |
| $\rho_P/\rho_\oplus$ | $1.53^{+0.07}_{-0.06}$ | $1.67^{+0.13}_{-0.12}$ | 1. |

might be an excellent target for transmission spectroscopy observations with current observatories.

For future *James Webb Space Telescope* (JWST) observations, the brightness of TOI-141 might impact on the type of observations that can be made *because the star is too bright*. However, observations with different instruments and filters might allow to characterize this exoplanet, especially at wavelengths $> 2\mu m$. For example, a wide range of *NIRCam* observations are possible to make for TOI-141b with a range of filters, which implies the thermal emission of this exoplanet might be easily detected with just one JWST transit. For transmission, *NIRISS+SOSS* observations will be possible for wavelengths $\gtrsim 1.5\mu m$ where the instrument saturation falls for magnitudes brigther than $J \sim 7$, allowing to target a wide range of possible molecular features for this exoplanet. In summary, thus, TOI-141b could be a prime target for JWST transit and occultation observations of hot super-Earths.

## 5   CONCLUSIONS

In this work, we have presented TOI-141b, a hot Super-Earth orbiting in a 1-day period around the G-type star HD 213885 — the second brightest star known to host an ultra-short period exoplanet. The exoplanet was detected by *TESS* photometry and later confirmed and further characterized using precise RV observations with the CORALIE, HARPS and FEROS spectrographs. Our observations reveal that TOI-141b has a rocky bulk composition, converting this exoplanet into a bona-fide super-Earth: a rocky planet with a bulk composition similar (although enhanced in iron) to Earth. In addition, our precise radial-velocity measurements reveal the presence of an additional Neptune-mass exoplanet, TOI-141c, on a 4.78-day orbit which does not show transits in the TESS photometry.

TOI-141b is an interesting exoplanet from the perspective of atmospheric characterization of hot super-Earths and especially to be compared with 55 Cancri e, for which TOI-141b is a very similar exoplanet. Characterization of this exoplanet with both present (e.g., HST, Spitzer) and future (e.g., JWST) space-based facilities might help unveil the nature of the atmospheres of these kind of exoplanets, allowing to kickstart comparative exoplanetology of hot super-Earths.

## APPENDIX A: AUTHOR AFFILIATIONS

[1] Space Telescope Science Institute, 3700 San Martin Drive, Baltimore, MD 21218, USA.
[2] Max-Planck-Institut für Astronomie, Königstuhl 17, 69117 Heidelberg, Germany.
[3] Center of Astro-Engineering UC, Pontificia Universidad Católica de Chile.
[4] Instituto de Astrofísica, Facultad de Física, Pontificia Universidad Católica de Chile.
[5] Facultad de Ingeniería y Ciencias, Universidad Adolfo Ibáñez, Av. Diagonal las Torres 2640, Peñalolén, Santiago, Chile.
Av. Vicuña Mackenna 4860, 782-0436 Macul, Santiago, Chile.
[6] Millennium Institute for Astrophysics, Santiago, Chile.
[7] University of Zurich, Institut of Computational Sciences, University of Zurich, Winterthurerstrasse 190, CH-8057, Zurich, Switzerland.
[8] Departamento de Astronomía, Universidad de Chile, Camino El Observatorio 1515, Las Condes, Santiago, Chile.
[9] Departamento de Ciencias Físicas, Facultad de Ciencias Exactas, Universidad Andrés Bello, Las Condes, RM, Santiago, Chile.
[10] NASA Ames Research Center, Moffett Field, CA, 94035.
[11] SETI Institute, Moffett Field, CA 94035, USA.
[12] Center for Astrophysics | Harvard & Smithsonian, 60 Garden Street, Cambridge, Massachusetts 02138, USA.
[13] Department of Physics, University of Warwick, Gibbet Hill Road, Coventry CV4 7AL.
[14] Centre for Exoplanets and Habitability, University of Warwick, Gibbet Hill Road, Coventry CV4 7AL.
[15] Instituto de Astrofísica e Ciências do Espaço, Universidade do Porto, CAUP, Rua das Estrelas, PT4150-762 Porto, Portugal.
[16] Depto. Astrofíisica, Centro de Astrobiología (CSIC-INTA), ESAC campus, Camino Bajo del Castillo s/n, 28692 Villanueva de la Cañada Madrid, Spain.
[17] Observatoire de l'Université de Genève, 51 chemin des Maillettes, 1290 Versoix, Switzerland.
[18] European Southern Observatory, Alonso de Cordova 3107, Vitacura Casilla 19001, Santiago 19, Chile.
[19] Departamento de Física e Astronomia, Faculdade de Ciências, Universidade do Porto, Rua do Campo Alegre, 4169-007 Porto, Portugal.
[20] Department of Physics and Kavli Institute for Astrophysics and Space Science, Massachusetts Institute of Technology, Cambridge, MA 02139, USA.
[21] Department of Astrophysical Sciences, Princeton University, Princeton, NJ 08544, USA.
[22] Department of Physics and Astronomy, University of Louisville, Louisville, KY 40292, USA.
[23] Computational Engineering and Science Research Centre, University of Southern Queensland, Toowoomba, QLD, 4350, Australia.
[24] Mt. Stuart Observatory, New Zealand.
[25] Dept. of Physics & Astronomy, Swarthmore College, Swarthmore PA 19081, USA.

[26] Nicolaus Copernicus Astronomical Center, Polish Academy of Sciences, ul. Rabiańska 8, 87-100 Toruń, Poland.
[27] Cerro Tololo Inter-American Observatory, National Optical Astronomical Observatory, Casilla 603, La Serena 1700000, Chile.
[28] Dunlap Institute for Astronomy and Astrophysics, University of Toronto, Ontario M5S 3H4, Canada.
[29] Department of Physics and Astronomy, University of North Carolina at Chapel Hill, Chapel Hill, NC 27599-3255, USA.
[30] Noqsi Aerospace Ltd, 15 Blanchard Ave., Billerica, MA 01821, USA.
[31] Exoplanets and Stellar Astrophysics Laboratory, Code 667, NASA Goddard Space Flight Center, Greenbelt, MD 20771, USA.
[32] Millenium Engineering.

## REFERENCES

Ambikasaran S., Foreman-Mackey D., Greengard L., Hogg D. W., O'Neil M., 2014
Angelo I., Hu R., 2017, AJ, 154, 232
Baranne A., Mayor M., Poncet J., 1979, Vistas in Astronomy, 23, 279
Batalha N. M., et al., 2011, ApJ, 729, 27
Bouchet J., Mazevet S., Morard G., Guyot F., Musella R., 2013, Physical Review B, 87, 094102
Bourrier V., et al., 2018, A&A, 619, A1
Brahm R., Jordán A., Espinoza N., 2017a, PASP, 129, 034002
Brahm R., Jordán A., Hartman J., Bakos G., 2017b, MNRAS, 467, 971
Brahm R., et al., 2018a, MNRAS,
Brahm R., et al., 2018b, MNRAS, 477, 2572
Buchner J., et al., 2014, A&A, 564, A125
Carrier F., Bourban G., 2003, A&A, 406, L23
Castelli F., Kurucz R. L., 2003, in Piskunov N., Weiss W. W., Gray D. F., eds, IAU Symposium Vol. 210, Modelling of Stellar Atmospheres. p. A20 (arXiv:astro-ph/0405087)
Collins K. A., Kielkopf J. F., Stassun K. G., Hessman F. V., 2017, AJ, 153, 77
Connolly J., 2009, Geochemistry, Geophysics, Geosystems, 10
Dai F., Masuda K., Winn J. N., 2018, ApJ, 864, L38
Dawson R. I., Fabrycky D. C., 2010, ApJ, 722, 937
Delgado Mena E., Israelian G., González Hernández J. I., Bond J. C., Santos N. C., Udry S., Mayor M., 2010, ApJ, 725, 2349
Demory B.-O., et al., 2016, Nature, 532, 207
Dorn C., Heng K., 2018, The Astrophysical Journal, 853, 64
Dorn C., Khan A., Heng K., Connolly J. A., Alibert Y., Benz W., Tackley P., 2015, Astronomy & Astrophysics, 577, A83
Dorn C., Venturini J., Khan A., Heng K., Alibert Y., Helled R., Rivoldini A., Benz W., 2017, Astronomy & Astrophysics, 597
Dorn C., Noack L., Rozel A., 2018, Astronomy & Astrophysics, 614, A18
Elsworth Y. P., Thompson M. J., 2004, Astronomy & Geophysics, 45, 5.14
Espinoza N., 2018, Research Notes of the AAS, 2, 209
Espinoza N., Kossakowski D., Brahm R., 2018, arXiv e-prints, p. arXiv:1812.08549
Feroz F., Hobson M. P., Bridges M., 2009, MNRAS, 398, 1601
Fischer D. A., et al., 2008, ApJ, 675, 790
Foreman-Mackey D., Agol E., Ambikasaran S., Angus R., 2017, AJ, 154, 220
Fulton B. J., Petigura E. A., Blunt S., Sinukoff E., 2018, PASP, 130, 044504
Gaia Collaboration et al., 2018, A&A, 616, A1

Henry T. J., Soderblom D. R., Donahue R. A., Baliunas S. L., 1996, AJ, 111
Holman M. J., Murray N. W., 2005, Science, 307, 1288
Huang C. X., et al., 2018, preprint, (arXiv:1809.05967)
Jenkins J. M., et al., 2016, in Software and Cyberinfrastructure for Astronomy IV. p. 99133E, doi:10.1117/12.2233418
Jensen E., 2013, Tapir: A web interface for transit/eclipse observability, Astrophysics Source Code Library (ascl:1306.007)
Kaufer A., Pasquini L., 1998, in D'Odorico S., ed., Proc. SPIEVol. 3355, Optical Astronomical Instrumentation. pp 844–854, doi:10.1117/12.316798
Kipping D. M., 2013, MNRAS, 435, 2152
Kite E. S., Manga M., Gaidos E., 2009, The Astrophysical Journal, 700, 1732
Knutson H. A., et al., 2014, ApJ, 794, 155
Korenaga J., 2010, The Astrophysical Journal Letters, 725, L43
Kovács G., Zucker S., Mazeh T., 2002, A&A, 391, 369
Kreidberg L., 2015, PASP, 127, 1161
Li J., Tenenbaum P., Twicken J. D., Burke C. J., Jenkins J. M., Quintana E. V., Rowe J. F., Seader S. E., 2019, Publications of the Astronomical Society of the Pacific, 131, 024506
Malavolta L., et al., 2018, AJ, 155, 107
Maxted P. F. L., et al., 2016, A&A, 591, A55
Mayor M., et al., 2003, The Messenger, 114, 20
Miguel Y., 2019, MNRAS, 482, 2893
Nelson B. E., Ford E. B., Buchner J., Cloutier R., Díaz R. F., Faria J. P., Rajpaul V. M., Rukdee S., 2018, preprint, (arXiv:1806.04683)
Neves V., Santos N. C., Sousa S. G., Correia A. C. M., Israelian G., 2009, A&A, 497, 563
Noack L., Breuer D., 2014, Planetary and Space Science, 98, 41
Petrovich C., Deibert E., Wu Y., 2018, preprint, (arXiv:1804.05065)
Queloz D., et al., 2001, The Messenger, 105, 1
Ricker G. R., et al., 2015, Journal of Astronomical Telescopes, Instruments, and Systems, 1, 014003
Sanchis-Ojeda R., Rappaport S., Winn J. N., Levine A., Kotson M. C., Latham D. W., Buchhave L. A., 2013, ApJ, 774, 54
Sanchis-Ojeda R., Rappaport S., Winn J. N., Kotson M. C., Levine A., El Mellah I., 2014, ApJ, 787, 47
Smith J. C., et al., 2012, PASP, 124, 1000
Sneden C., 1973, ApJ, 184, 839
Stassun K. G., et al., 2018, AJ, 156, 102
Stixrude L., Lithgow-Bertelloni C., 2011, Geophysical Journal International, 184, 1180
Stumpe M. C., et al., 2012, PASP, 124, 985
Stumpe M. C., Smith J. C., Catanzarite J. H., Van Cleve J. E., Jenkins J. M., Twicken J. D., Girouard F. R., 2014, PASP, 126, 100
Tokovinin A., 2018, Publications of the Astronomical Society of the Pacific, 130, 035002
Tsiaras A., et al., 2016, ApJ, 820, 99
Twicken J. D., et al., 2018, PASP, 130, 064502
Valencia D., OÂŠconnell R. J., Sasselov D. D., 2007, The Astrophysical Journal Letters, 670, L45
Van Heck H., Tackley P., 2011, Earth and Planetary Science Letters, 310, 252
Vanderplas J., Connolly A., Ivezić Ž., Gray A., 2012, in Conference on Intelligent Data Understanding (CIDU). pp 47 –54, doi:10.1109/CIDU.2012.6382200
Winn J. N., et al., 2011, ApJ, 737, L18
Winn J. N., Sanchis-Ojeda R., Rappaport S., 2018, preprint, (arXiv:1803.03303)
Yi S., Demarque P., Kim Y.-C., Lee Y.-W., Ree C. H., Lejeune T., Barnes S., 2001, ApJS, 136, 417
Zechmeister M., Kürster M., 2009, A&A, 496, 577
Zeng L., Sasselov D. D., Jacobsen S. B., 2016, ApJ, 819, 127

This paper has been typeset from a TEX/LATEX file prepared by the author.